

WHAM: A WENO-based general relativistic numerical scheme I: Hydrodynamics

Alexander Tchekhovskoy,^{1*} Jonathan C. McKinney,^{2*} Ramesh Narayan^{2*}

¹*Harvard-Smithsonian Center for Astrophysics, 60 Garden Street, MS 10, Cambridge, MA 02138, USA*

²*Institute for Theory and Computation, Harvard-Smithsonian Center for Astrophysics, 60 Garden Street, MS 51, Cambridge, MA 02138, USA*

Accepted 2007 April 18. Received 2007 April 3; in original form 2006 December 29

ABSTRACT

Active galactic nuclei, x-ray binaries, pulsars, and gamma-ray bursts are all believed to be powered by compact objects surrounded by relativistic plasma flows driving phenomena such as accretion, winds, and jets. These flows are often accurately modelled by the relativistic magnetohydrodynamics (MHD) approximation. Time-dependent numerical MHD simulations have proven to be especially insightful, but one regime that remains difficult to simulate is when the energy scales (kinetic, thermal, magnetic) within the plasma become disparate. We develop a numerical scheme that significantly improves the accuracy and robustness of the solution in this regime. We use a modified form of the WENO method to construct a finite-volume general relativistic hydrodynamics code called WHAM that converges at fifth order. We avoid (1) field-by-field decomposition by adaptively reducing down to 2-point stencils near discontinuities for a more accurate treatment of shocks, and (2) excessive reduction to low order stencils, as in the standard WENO formalism, by maintaining high order accuracy in smooth monotonic flows. Our scheme performs the proper surface integral of the fluxes, converts cell averaged conserved quantities to point conserved quantities before performing the reconstruction step, and correctly averages all source terms. We demonstrate that the scheme is robust in strong shocks, very accurate in smooth flows, and maintains accuracy even when the energy scales in the flow are highly disparate.

Key words: accretion, accretion discs – black hole physics – galaxies: jets – hydrodynamics – magnetohydrodynamics (MHD) – methods: numerical

1 INTRODUCTION

Astrophysical systems containing compact objects are the brightest and most efficient engines in the Universe. Enormous amounts of energy in the form of radiation and outflows are released by accreting black hole systems at the heart of active galactic nuclei (AGN, Krolik 1999), gamma-ray bursts (GRBs, Woosley 1993), and black hole X-ray binaries (XRBs, Lewin et al. 1995). Pulsars and their associated plerions are powered by the relativistic spin-down of highly magnetized neutron stars (Goldreich & Julian 1969). These systems involve strong magnetic fields, relativistic flows, and strong gravity. A general framework that has proven to be accurate in this regime is the ideal magnetohydrodynamic approximation (MHD) (Phinney 1983).

Significant uncertainty has remained in how black hole

accretion systems are powered and produce relativistic jets. Several seminal works have outlined plausible key mechanisms. Balbus & Hawley (1991) showed that the magnetorotational instability (MRI) drives the turbulent transport of angular momentum within an accretion disk. The MRI generates a dynamo that amplifies any weak magnetic field in the accreting plasma. Blandford & Payne (1982) found self-similar MHD solutions that describe winds launched magnetocentrifugally from thin magnetized accretion disks. Blandford & Znajek (1977) described a model that shows how black hole spin energy could be used to power a relativistic jet. Despite these important advances, it remains unclear how the various mechanisms coexist and how effective they are in real astrophysical systems.

Time-dependent numerical simulations have demonstrated that an accreting rotating black hole produces a disc wind and a pair of relativistic jets as a *natural* outcome of quasi-steady magnetized disc accretion. De Villiers et al. (2003) identified the general morphology of black hole accretion flows to consist of a disk, a

* E-mail: atchekho@cfa.harvard.edu (AT);
jmckinney@cfa.harvard.edu (JCM);
rmarayan@cfa.harvard.edu (RN)

corona, a coronal outflow, and an evacuated funnel where the magnetized jet develops. McKinney & Gammie (2004) showed that the magnetized funnel jet is well-described by the Blandford & Znajek solution. Following up on the pioneering simulations by Koide et al. (2002) and Koide (2003), Komissarov (2005) showed that even without a disk the natural outcome is that black hole spin energy is extracted via the Blandford & Znajek effect. Hirose et al. (2004) and McKinney (2005) showed that the field geometry associated with the Blandford-Znajek effect is the most stable large-scale field geometry in the presence of a turbulence disk around a black hole. Komissarov & McKinney (2007) showed that the Blandford-Znajek effect operates even for $a = 1$ despite concerns that at high black hole spin the field might get expelled from the horizon. McKinney (2006b) demonstrated that the disc models studied by De Villiers et al. (2003) and McKinney & Gammie (2004) produce a self-consistent magnetized jet with a Lorentz factor of $\gamma \sim 10$ and an opening angle of $\theta \sim 5^\circ$, demonstrating that the ideal MHD approximation is sufficient to explain many relativistic astrophysical jets. Finally, McKinney & Narayan (2007a,b) showed that the Blandford-Payne magnetically-driven wind does not properly describe the wind from turbulent disks near black holes and that the low density magnetized jet from the black hole is collimated by the disk corona and wind rather than being self-collimated.

Many of the results described above were obtained from simulations that used numerical methods based upon so-called ‘conservative schemes,’ which have been proven to be accurate and robust for modeling relativistic flows (Aloy et al. 1999, 2000; Font 2003; Martí & Müller 2003; Leismann et al. 2004; Aloy et al. 2005). The main advantage of these schemes is that they conserve the integrals of motion up to machine precision, and this explicit conservation enables them to accurately resolve discontinuities in the flow. However, systems with kinetic, thermal, or magnetic energy scales differing by orders of magnitude pose serious difficulties for conservative numerical schemes. This happens in, e.g., highly supersonic jets and winds where the internal energy is much smaller than the kinetic energy. Since conservative schemes evolve the values of momenta and total energy (the sum of the kinetic, internal, and magnetic energies), even a relatively small error in the evolution of these quantities can destroy the accuracy of such flows. In the hydrodynamic case, this is referred to as the high Mach number problem (Ryu et al. 1993; Feng et al. 2004). A similar problem occurs in the highly magnetized MHD regime, where the equations become stiff when the effective magnetic ‘Mach’ number $M_{\text{mag}} \equiv \sqrt{\sigma} \gg 1$, where σ is the comoving magnetic energy density per unit rest mass energy density. In this paper we focus on solving the hydrodynamic high Mach number problem, although the ultimate goal is to eventually apply our method to the MHD equations to study black hole and neutron star systems that may have $M_{\text{mag}} \gtrsim 10^3$.

There are alternatives to evolving the total energy equation and some of them provide a reasonably accurate treatment of high Mach number flows. One can use a ZEUS-type method (Stone & Norman 1992) that solves the internal energy evolution equation with an artificial viscosity (e.g., Hawley 2000; Igumenshchev et al. 2003; De Villiers & Hawley 2003). However, the schemes

by Hawley (2000); De Villiers & Hawley (2003) lose energy generated in reconnecting current sheets and the scheme by Igumenshchev et al. (2003), which uses an artificial resistivity, still does not strictly conserve energy. Bucciantini et al. (2006) employ a method that solves the entropy evolution equation and does not allow any shocks in the solution.

Another approach is the ‘dual-energy formalism’ that involves switching from evolving the total energy to evolving the internal energy (or entropy) equations of motion for a Mach number larger than a threshold value M_{th} . For instance, $M_{\text{th}} \sim 10$ for Ryu et al. (1993), $M_{\text{th}} \sim 5$ for Bryan et al. (1995), and $M_{\text{th}} \sim 50$ for Feng et al. (2004). For example, Ryu et al. (1993) switch from evolving the energy to evolving the entropy equation when (1) the Mach number is greater than ~ 10 and (2) either the shock strength is $\lesssim 1/3$ or the flow is diverging. This criterion can fail to capture the flow properly in the presence of weak shocks (which could dominate the energy dissipation). Also, once the entropy equation is used to determine the pressure, the pressure could be secularly underestimated if a shock is building up.

Finally, there are Lagrangian-type schemes such as by Trac & Pen (2004), who use a moving grid technique for treating high Mach number flows (see section 5.2 for further discussion). However, their scheme requires a sophisticated treatment of the advection terms in the equation of motion. There also exist specialized schemes that are independent of the Mach number (Mary et al. 2000).

We describe a general relativistic hydrodynamic scheme that solves the total energy equation yet provides an accurate and robust solution in the difficult regime of high Mach number flows. This is achieved by (1) being finite-volume (conserves integrals of motion to machine accuracy), (2) being fifth order accurate, (3) maintaining fifth order accuracy in monotonic regions (which avoids the excessive reduction that occurs in the standard WENO formalism), (4) using adaptive stencil reduction near discontinuities, and (5) obtaining fluxes from reconstruction of primitive, rather than e.g. conserved, quantities. Our scheme performs the proper surface integral of the fluxes and converts cell averaged conserved quantities to point conserved quantities before the reconstruction step. It also averages the source terms that appear on the right hand side of the conservation equations. These averaging and de-averaging procedures enable our scheme to have an error term that is fifth order in grid cell spacing for an arbitrary metric and coordinate system. Our scheme uses a modified form of the WENO method (see, e.g., Shu 1997) for spatial discretisation and the method of lines approach (see, e.g., LeVeque 1991) with Runge-Kutta stepping (Press et al. 1992; Shu 1997) for time discretisation. We eliminate the expensive eigenvector decomposition step used by other high order methods by adaptively reducing down to 2-point stencils in the vicinity of discontinuities. This reduction technique gives a similar accuracy to eigenvector decomposition without the additional computational expense. On the other hand by maintaining high order accuracy in smooth monotonic flows, we are able to avoid excessive reduction to low order stencils that occurs in the standard WENO formalism.

Our numerical scheme is called WHAM, which stands for WENO high accuracy magnetohydrodynamics. In sec-

tion 2 we describe the equations that determine the relevant physics (ideal MHD, single fluid approximation) in the form used by the scheme. This is followed by a detailed description of the finite-volume numerical scheme in section 3 and of the fifth order WENO-type reconstruction procedure in section 4. Section 5 presents results of an extensive set of tests for code verification. Section 6 describes the limitations of the numerical scheme, section 7 outlines some possible applications, and section 8 summarizes our results and concludes. In the Appendix we describe the method for reducing the stencil size near discontinuities, preserving the fifth order of reconstruction in monotonic regions, and other implementation details.

2 GOVERNING GRMHD EQUATIONS

While this paper focuses on a new purely hydrodynamical numerical scheme, many of the tools we develop can be applied to a full MHD scheme. Therefore we keep our discussion as general as possible. Here we outline the general relativistic magnetohydrodynamic (GRMHD) equations of motion in the form of conservation laws. Throughout, we use the Einstein summation convention, where Greek letters run from 0 to 3 and Latin letters from 1 to 3. The units are such that $G = c = 1$.

The continuity equation that describes baryon number conservation is given by

$$(\rho u^\mu)_{;\mu} = 0, \quad (1a)$$

where ρ is mass density in the fluid frame, u^μ is the 4-velocity of the fluid and the ‘ $;$ ’ subscript denotes the covariant derivative with respect to x^μ . The energy-momentum conservation equation is given by

$$T^\mu{}_{\nu;\mu} = 0, \quad (1b)$$

where $T^{\mu\nu}$ are the components of the energy-momentum tensor. Finally, the source-free part of Maxwell’s equations describes the evolution of the fields,

$${}^*F^{\mu\nu}{}_{;\nu} = 0, \quad (1c)$$

where ${}^*F^{\mu\nu} = 1/2 \epsilon^{\mu\nu\kappa\lambda} F_{\kappa\lambda}$ are the components of the dual of the electromagnetic tensor (Misner et al. 1973).

The energy-momentum tensor can be written as a sum of matter and electromagnetic contributions, $T^{\mu\nu} = T_{\text{MA}}^{\mu\nu} + T_{\text{EM}}^{\mu\nu}$, with

$$T_{\text{MA}}^{\mu\nu} = (\rho + u_g + p_g)u^\mu u^\nu + p_g g^{\mu\nu}, \quad (2)$$

$$T_{\text{EM}}^{\mu\nu} = F^{\mu\kappa} F^\nu{}_\kappa - 1/4 g^{\mu\nu} F^{\kappa\lambda} F_{\kappa\lambda}, \quad (3)$$

where u_g and p_g are the internal energy and pressure in the fluid frame, and $F^{\mu\nu}$ is the electromagnetic field tensor. Introducing the moving magnetic field 4-vector, $b^\nu = u_\mu {}^*F^{\mu\nu}$, in ideal MHD it can be shown that

$$T^\mu{}_\nu = (\rho + u_g + p_g + b^2)u^\mu u_\nu + (p_g + 1/2 b^2) \delta^\mu{}_\nu - b^\mu b_\nu \quad (4)$$

(Gammie et al. 2003).

For numerical purposes we write down equations (1a) – (1c) in a coordinate basis. The continuity equation (1a) takes the form (Landau & Lifshitz 1975),

$$\partial_t(\sqrt{-g}\rho u^t) + \partial_i(\sqrt{-g}\rho u^i) = 0, \quad (5a)$$

where $g = \text{Det } g_{\mu\nu}$ is the metric determinant and the ‘ t ’

index denotes the time component. Similarly, the energy-momentum equation (1b) takes the form

$$\partial_t(\sqrt{-g}T^t{}_\nu) + \partial_i(\sqrt{-g}T^i{}_\nu) = \sqrt{-g}T^\kappa{}_\lambda \Gamma^\lambda{}_{\nu\kappa}, \quad (5b)$$

where $\Gamma^\lambda{}_{\nu\kappa}$ are the connection coefficients. Finally, with the introduction of 3-vectors of magnetic and electric fields, $B^i \equiv {}^*F^{it}$ and $E^i \equiv F^{it}/\sqrt{-g}$, equation (1c) is equivalent to the induction equation,

$$\begin{aligned} \partial_t(\sqrt{-g}B^i) &= -\partial_j[\sqrt{-g}(\epsilon^{ijk}E_k)] \\ &= -\partial_j[\sqrt{-g}(B^i v^j - B^j v^i)], \end{aligned} \quad (5c)$$

where $v^i = u^i/u^t$ is the 3-velocity, plus the no-monopoles constraint,

$$\partial_i(\sqrt{-g}B^i) = 0. \quad (5d)$$

In deriving the last equality in equation (5c) we have used the ideal MHD approximation $E_i = -\epsilon_{ijk}v^j B^k \equiv -(\mathbf{v} \times \mathbf{B})_i$.

Equations (5a)–(5d) determine the evolution of a plasma system for given initial and boundary conditions. We derive numerical discretisations of these equations in the next section.

3 NUMERICAL SCHEME

We develop a numerical scheme based upon a solution to a general set of conservation laws.

3.1 Vector form of conservation laws

The equations of motion (5a)–(5c) can be written in the form of a vector conservation law:

$$\partial_t \mathbf{U}(\mathbf{P}) + \partial_i \mathbf{F}^i(\mathbf{P}) = \mathbf{S}(\mathbf{P}), \quad (6)$$

where the vector of conserved quantities is

$$\mathbf{U}(\mathbf{P}) \equiv \sqrt{-g}(\rho u^t, T^t{}_t + \rho u^t, T^t{}_j, B^k), \quad (7)$$

the vector of fluxes in the i th direction is

$$\mathbf{F}^i(\mathbf{P}) \equiv \sqrt{-g}(\rho u^i, T^i{}_t + \rho u^i, T^i{}_j, B^i v^k - B^k v^i), \quad (8)$$

and the vector of source terms is

$$\mathbf{S}(\mathbf{P}) \equiv \sqrt{-g}(0, T^\nu{}_\lambda \Gamma^\lambda{}_{\mu\nu}, 0, 0, 0), \quad (9)$$

where, according to the convention, i, j, k run from 1 to 3 and λ, μ, ν run from 0 to 3 so the vectors \mathbf{U} , \mathbf{F}^i , and \mathbf{S} have 8 components each. We have analytically removed the mass energy density from the conserved quantity that corresponds to the total energy, the second component of \mathbf{U} , so that the method remains accurate in the limit of nonrelativistic flows (see Appendix A9). As a set of primitive quantities we choose

$$\mathbf{P} \equiv (\rho, u_g, \tilde{u}^j, B^k), \quad (10)$$

where the spatial components of the relative 4-velocity $\tilde{u}^j \equiv u^j - \gamma \eta^j$, in which $\gamma = -u^\mu \eta_\mu$ is the Lorentz factor of the flow as measured in the normal observer frame, and $\eta_\mu = (-\alpha, 0, 0, 0)$ is the 4-velocity of a zero angular momentum observer in the coordinate basis for axisymmetric space-times; here $\alpha = (-g^{tt})^{-1/2}$ (Noble et al. 2006). One

can show that $\tilde{u}^t = 0$ and $\gamma = \sqrt{1 + \tilde{u}^i \tilde{u}_i}$. Using the relative 4-velocity (as compared to the usual 4-velocity) has 2 advantages: (1) its interpolation always leads to a physical state and (2) even in rotating (e.g., Kerr) space-times its spatial components determine the unique value of $u^t = \gamma/\alpha$.

Note that system (6) does not contain the no-monopoles constraint (5d). This constraint is considered in future work, see section 6.

3.2 Motivation for a consistent finite volume scheme

Eulerian conservative numerical schemes keep track of the values of conserved quantities for each grid cell. In this section we show the importance of accounting for the difference between the cell averaged and cell centred values of these quantities for maintaining high accuracy in studies of highly supersonic hydrodynamic flows. In such flows small relative errors in the total energy can lead to large relative errors in the internal energy. This is known as the high Mach number problem (Ryu et al. 1993; Trac & Pen 2004; Feng et al. 2004). We show that even though the errors are second order in grid cell spacing, their magnitude is proportional to the square of the Mach number and so these errors can destroy the accuracy of numerical models.

Consider a numerical method based upon piecewise linear interpolations of primitive quantities, and consider a flow in which $\rho \propto \text{const}$, $v \propto x$, and the internal energy is negligible relative to the kinetic energy, $u_g \ll \rho v^2$. Is a linear interpolation of the conserved energy then sufficient? That is, can we assume that there is a negligible difference between $E(x) = \rho v^2/2 + u_g \propto x^2$ at the centre $x = x_i$ of a grid cell, and its average value $\langle E \rangle$ over that grid cell? The answer is we cannot since for $E(x)$ defined above,

$$\langle E \rangle - E = \frac{1}{24} E''(x_i) \Delta x^2 = \frac{1}{24} \rho v^2 \Big|_{x=\Delta x} \gg u_g, \quad (11)$$

where Δx is the grid cell spacing. Neglecting the difference between E and $\langle E \rangle$ will manifest as a significant error in the smaller quantity u_g .

In particular, consider a simple nonrelativistic one-dimensional, high Mach number hydrodynamic flow (no gravity or any other external forces). Suppose initially the flow has a uniform density and pressure, and its velocity is a linear function of position. We call this a Hubble-type flow. The primitive flow variables (density, velocity, and specific internal energy) at time t are given by:

$$\begin{aligned} \rho(x, t) &= \frac{\rho_0}{1 + v'_0 t}, \\ v(x, t) &= \frac{v'_0 x}{1 + v'_0 t}, \\ u_g(x, t) &= \frac{u_0}{(1 + v'_0 t)^\Gamma}, \end{aligned} \quad (12)$$

where $v'_0 \equiv dv/dx(x, t = 0)$. We assume the equation of state $p_g = (\Gamma - 1)u_g$, where Γ is the adiabatic index of the gas, and we choose the flow parameters ρ_0 , u_0 , and v'_0 such that the flow is highly supersonic in the grid cell centres, $u_g \ll \rho v^2$.

As we show in Appendix A1, if one discretises the above equations in space and time to any order but neglects the difference between E and $\langle E \rangle$, then after one time step one

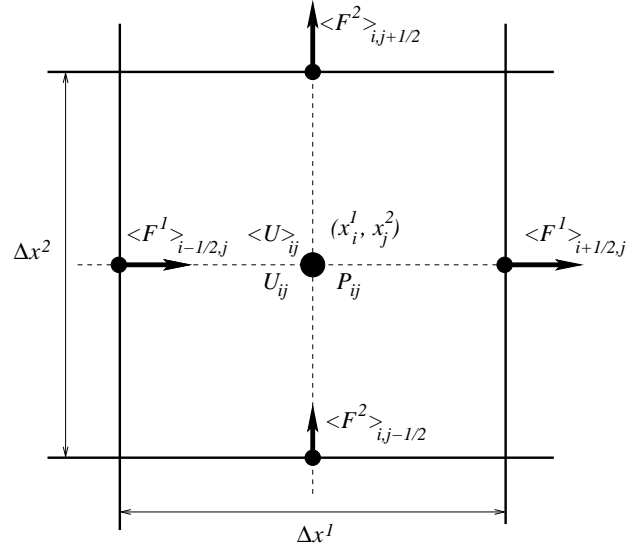


Figure 1. Location of quantities within the grid cell Δ_{ij} . Thick solid lines show the grid of cell interfaces and dashed lines show the grid of cell centres. The cell centre is indicated by the large dot where the primitive P_{ij} , point conserved U_{ij} , and average conserved $\langle U \rangle_{ij}$ quantities are located. The fluxes are located at the centres of grid cell interfaces shown by smaller dots. See sections 3.3 – 3.4.

makes a relative error in internal energy,

$$\frac{\mathcal{E}(u_g)}{u_0} \sim -M_{\min}^2 \delta t, \quad (13)$$

where $M_{\min}^2 \sim \rho_0 v_0'^2 \Delta x^2 / u_0$ is the square of the minimal value of the Mach number on the grid, Δx is the grid cell size, and $\delta t = v_0' \Delta t$ is the dimensionless time step for the problem for a computational box with outer edge $x = 1$.

At every time step the internal energy uniformly decreases by more than it should and after several time steps the error will be quite large, and u_g may even become negative. Even though this error in the internal energy is second order in space, the coefficient of this error is proportional to the Mach number of the flow squared. Therefore, for a large Mach number, any scheme that does not distinguish between cell averaged and point conserved quantities has to use a resolution proportional to the Mach number of the flow in order to correctly capture the evolution of the internal energy over the relevant timescale of $\delta t \sim 1$. For instance, for $M_{\min} = 100$ such a scheme requires roughly a 100x resolution increase. See section 5.1 for a numerical verification of these statements.

3.3 Numerical grid

The numerical scheme is built upon a uniform grid in a coordinate basis, where for simplicity we consider here the two-dimensional case (the three-dimensional case is a trivial extension – also see section 6). The grid consists of cells that we define as $\Delta_{ij} = (x_{i-1/2}^1, x_{i+1/2}^1) \times (x_{j-1/2}^2, x_{j+1/2}^2)$, where $(x_i^1, x_j^2, t_n) = (i\Delta x^1, j\Delta x^2, n\Delta t)$, Δx^1 and Δx^2 are the cell spacings (see figure 1), and Δt is the time step. For a discussion of numerical grid generation, see Thompson et al. (1985).

An arbitrary smooth transformation can be used to map this computational grid into physical space as a fixed adaptive mesh that focuses on the regions of interest (for more detail, see Gammie et al. 2003). The transformation of any tensorial quantity requires derivatives of the coordinate map that are either computed analytically or using a simple numerical scheme that results in an accuracy of roughly the machine accuracy to the 2/3 power (Press et al. 1992). A similar method is used to compute the connection coefficients. Therefore the metric identities are of similar accuracy. Both the discretisation of equations of motion and the reconstruction of functions are independent of the physical coordinates, and this makes the algorithm simple and general.

3.4 Finite volume discretisation of the equations

In this section we derive a finite volume discretisation of the conservation equations (6) for a two-dimensional problem. This discretisation guarantees that the integrals of motion are conserved up to machine precision error. Integrate any component of the vector equation (6) over a grid cell $V = \Delta_{ij}$ to obtain

$$\iint_V \frac{\partial U}{\partial t} dx^1 dx^2 + \iint_V \frac{\partial F^1}{\partial x^1} dx^1 dx^2 + \iint_V \frac{\partial F^2}{\partial x^2} dx^1 dx^2 = \iint_V S dx^1 dx^2. \quad (14)$$

Taking the integrals and dividing by grid cell volume $\Delta x^1 \Delta x^2$, we obtain a system of semi-discrete equations (method of lines, see e.g. LeVeque 1991):

$$\frac{\partial \langle U \rangle_{ij}}{\partial t} + \frac{\langle F^1 \rangle_{i+1/2,j} - \langle F^1 \rangle_{i-1/2,j}}{\Delta x^1} + \frac{\langle F^2 \rangle_{i,j+1/2} - \langle F^2 \rangle_{i,j-1/2}}{\Delta x^2} = \langle S \rangle_{ij}, \quad (15)$$

where the angle brackets denote spatial averaging over the volume/surface of the grid cell for quantities located inside/at the surface of the grid cell (Figure 1). So far this equation is exact.

We use Runge-Kutta 4th order accurate time stepping (RK-4, see Press et al. 1992) for discretising the system of ordinary differential equations (15) in time. Each Runge-Kutta trial step is a first order numerical discretisation of equation (15) given by:

$$\frac{\langle U \rangle_{ij}^{n+1} - \langle U \rangle_{ij}^n}{\Delta t} + \frac{\langle F^1 \rangle_{i+1/2,j} - \langle F^1 \rangle_{i-1/2,j}}{\Delta x^1} + \frac{\langle F^2 \rangle_{i,j+1/2} - \langle F^2 \rangle_{i,j-1/2}}{\Delta x^2} = \langle S \rangle_{ij}. \quad (16)$$

The RK-4 algorithm combines a series of four first-order trial time steps, which we refer to as substeps, with different Δt 's to obtain a 4th order accurate analog of (16). We note that formally we need to use RK-5 time stepping in order for our scheme to converge at fifth order. However, for most problems RK-4 produces time stepping errors that are much smaller than the truncation errors due to spatial reconstruction, so RK-4 is practically sufficient for attaining fifth order convergence (c.f. section 5.4 and Zhang & MacFadyen 2006,

hereafter ZM06; however, see section 5.1). We find that RK-4 always gives more accurate results than the RK-3 scheme from Shu (1997), for both smooth and discontinuous flows. We solve each Runge-Kutta substep given by equation (16) using the Godunov technique.

3.5 High-order Godunov schemes

Godunov schemes perform the evolution in time of a set of grid cell averages of conserved quantities, $\{\langle \mathbf{U} \rangle_{ij}^n\}$, by considering binary interactions between adjacent cells. These interactions are usually approximated to be one-dimensional. In the simplest case, the first order Godunov scheme, the distribution of conserved quantity inside each grid cell is assumed to be a constant. The one-dimensional interaction between two such distributions is the classical *Riemann problem*: the decay of a discontinuity between two *constant* distributions (Toro 1997). For a given discontinuity, an exact or approximate *Riemann solution* is obtained for the flux used to update the conserved quantity and obtain $\{\langle \mathbf{U} \rangle_{ij}^{n+1}\}$ at $t = t_{n+1}$. These first order schemes are robust but inaccurate for smooth flows or flows with discontinuities not modelled by the Riemann solver.

Higher-order Godunov schemes attempt to obtain higher accuracy by using higher order methods to compute both the interface states and the temporal updates. High-order methods are desirable since typically their computational cost is much less compared to increasing the numerical resolution for first order schemes. Higher-order Godunov numerical schemes generate a discontinuity at each interface as a result of a high-order reconstruction within adjacent grid cells (see section 4). The left/right interface states are fed to the Riemann solver that is used to obtain the flux at the interface. However, such Riemann solutions actually assume the distributions are *constant* within each cell and that the characteristics of the Riemann fan are linear (see, e.g., Colella & Woodward 1984; Mignone et al. 2005; Zhang & MacFadyen 2006). For example, one of the most advanced reconstruction schemes is the PPM scheme (Colella & Woodward 1984) where the left/right states (fed to a standard Riemann solver) are obtained by an average over a 'domain-of-dependence.' This averaging partially accounts for the left/right distributions being parabolic, but it still assumes the characteristics are linear.

Since high-order schemes actually generate *non-constant* distributions in each cell, the Riemann fan is non-linear and so standard Riemann solvers give an incorrect flux at the interface. This inconsistency leads to incorrect eigenwave amplitudes and potentially to spurious oscillations. In order to compute a Riemann solution consistently with the high-order scheme, one should instead solve the *Generalized Riemann Problem* (GRP, Section 13.4.1 from Toro 1997) that involves non-constant background distributions and so curved characteristics for the Riemann fan (see also Toro & Titarev 2006). However, using standard Riemann solvers may be sufficiently accurate for most problems. For simplicity, like most other schemes, WHAM uses such a standard Riemann solver.

3.6 Algorithm outline

We now describe our implementation of a consistent finite volume scheme, where by consistent we mean the numerical method takes into account the differences between point and average conserved quantities, fluxes, and source terms. Performing the conversion between cell averaged and cell centred values of conserved quantities is crucial for any test problem with disparate energy scales, e.g. high Mach number flows. In sections 3.2, 5.1, 5.2, 5.3, and 5.10 we give examples of highly supersonic flows that illustrate the importance of accounting for this difference.

The general procedure of our method is outlined below and can be used with any definition of the cell centre to interface reconstruction, the averaging and de-averaging of conserved quantities, the averaging of fluxes, and the averaging of source terms. Our particular reconstruction methods are described in section 4.

We subdivide the grid into three domains, denoted by Roman numerals in figure 2. In the standard boundary domain I the primitive quantities are specified by boundary conditions and in the standard computational domain III the conserved quantities are evolved. We also introduce an additional intermediate domain II where both the conserved quantities are evolved *and* the values of primitive quantities are specified according to the boundary conditions. This technique allows our boundary routines to work only with the primitive quantities in both the original boundary domain I and the intermediate boundary domain II. Without this additional domain our scheme would require applying the boundary conditions on the conserved quantities as well. Thus, the introduction of domain II simplifies our boundary condition routines, including those that involve parallel computation. As in the HARM code (Gammie et al. 2003), our scheme is parallelized using domain decomposition within the Message Passing Interface (MPI). For reasonably chosen resolutions per CPU (e.g. 32^2 to 64^2) we achieve no less than 70% parallel efficiency for 256 CPUs for 2D problems on a cluster with dual 2.0 GHz Opteron processors connected by Gigabit ethernet.

The initial conditions are set in domain III (active grid cells), where we define primitive quantities at cell centres, $\{\mathbf{P}_{ij}^0\}$. The boundary conditions for primitive quantities are set in domains I & II (boundary grid cells). In domains I – III, we then convert the point primitive quantities to point conserved quantities $\{\mathbf{U}_{ij}^0\}$. In domains II & III, the conserved quantities are either numerically or analytically averaged over grid cells to obtain $\{\langle\mathbf{U}\rangle_{ij}^0\}$.

The cell-averaged conserved quantities are evolved in time in domains II & III by a sequence of Runge-Kutta substeps given by (16). For each Runge-Kutta substep the cell-centered primitive quantities $\{\mathbf{P}_{ij}^{n+1}\}$ and cell-averaged conserved quantities $\{\langle\mathbf{U}\rangle_{ij}^{n+1}\}$ at the new time t_{n+1} are found from previously computed cell-centered primitive quantities $\{\mathbf{P}_{ij}^n\}$ and cell-averaged conserved quantities $\{\langle\mathbf{U}\rangle_{ij}^n\}$ (defined to be at time t_n) by the below procedure:

Step i. Using the cell centre to interface reconstruction on cell centred values of primitive quantities $\{\mathbf{P}_{ij}^n\}$, obtain their values on both sides of every cell interface in domains II & III, e.g. $\mathbf{P}_{i+1/2-0,j}^n$ and $\mathbf{P}_{i+1/2+0,j}^n$ for the interface $(i + 1/2, j)$;

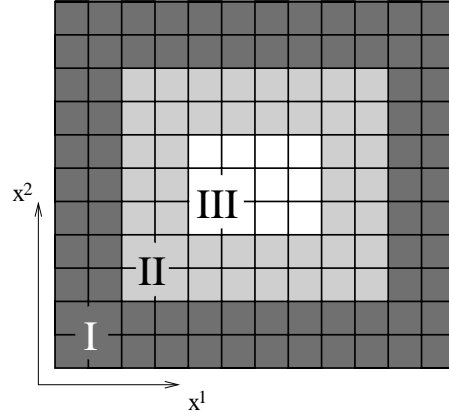


Figure 2. Computational grid for an illustrative 4×3 resolution. Grid cells are shown as squares with cell centres being the centres of these squares. Upon initialization we set the values of primitive quantities in the white grid squares (domain III, active grid cells) according to the initial conditions and in the dark and light shaded squares (domains I and II, the boundary cells) according to the boundary conditions; additionally, in domains II and III we compute the average values of conserved quantities either analytically or numerically. For domains II and III, at every time step we interpolate the primitive quantities from cell centres to cell interfaces to obtain the inter-cell fluxes, average them over the cell faces, and update the average values of conserved quantities in these domains. Finally, in domain III, we obtain the values of primitive quantities by converting the average values of conserved quantities to point values. In domains I & II the primitive quantities are set using the boundary conditions. The size of the white active grid cells region can be arbitrarily large (only limited by memory and speed considerations), whereas the width of the boundary cell layer surrounding it (shaded regions) only depends on the order of the scheme used.

Step ii. Using the approximate HLL Riemann solver (Gammie et al. 2003), obtain the flux at the centre of each interface in domains II & III, e.g., $\mathbf{F}_{i+1/2,j}^1(\mathbf{P}_{i+1/2-0,j}^n, \mathbf{P}_{i+1/2+0,j}^n)$;

Step iii. Spatially average the flux through every interface in domains II & III, using the centre to average reconstruction, to obtain, e.g., $\langle\mathbf{F}^1\rangle_{i+1/2,j}$;

Step iv. Find the point values of source terms in domains I – III, S_{ij} , according to equation (9);

Step v. Average the point values of source terms over grid cells, using the centre to average reconstruction, to obtain the cell-averaged values of source terms in domains II & III, $\langle S \rangle_{ij}$;

Step vi. Compute the cell-averaged conserved quantities at the new time in domains II & III, $\{\langle\mathbf{U}\rangle_{ij}^{n+1}\}$, by equation (16);

Step vii. De-average the conserved quantities, using the average to centre reconstruction, to obtain the point values $\{\mathbf{U}_{ij}^{n+1}\}$, located at grid cell centres, in domain III;

Step viii. Obtain the corresponding set of primitive quantities $\{\mathbf{P}_{ij}^{n+1}\}$ using a primitive variable solver Mignone & McKinney (2007);

Step ix. Apply the boundary conditions on the primitive quantities to get their values at grid cell centres in domains I & II;

We refer to the above algorithm as the WHAM scheme. For the purpose of demonstrating the importance of dis-

tinguishing between average and point values, we also consider an inconsistent scheme WENO-IFV that is the same as WHAM except we disable the averaging and de-averaging procedures (in the initial conditions and in Step iii, Step v, and Step vii). We also consider yet another scheme, denoted as the WHAM-IS scheme, for which we disable only the source integration by skipping Step v. This enables us to determine the effect of not averaging the source terms.¹

A feature of our finite volume approach is that conserved quantities are conserved to machine precision for all time. An alternative is to use the finite difference approach that evolves the cell centred point values of conserved quantities, so that the conserved quantities are then conserved to truncation error (Shu 1997). While the finite difference approach can be made to account for the difference between averaged and point values of conserved quantities, we find that it is less robust than the finite volume method we have described and less desirable since it does not conserve the proper quantities.

4 RECONSTRUCTION

In this section we explain the method WHAM uses to perform the cell centre to interface reconstruction in Step i, the averaging in Step iii and Step v, and the de-averaging in Step vii.

4.1 Quantities to reconstruct

High-order schemes are built upon reconstructing some set of quantities from the cell centre to the cell interface. Commonly either the primitive or conserved quantities are chosen to be interpolated to obtain the interface state. We perform the cell centre to interface reconstruction on density and internal energy, and for the reconstruction of velocity we use a procedure that is more robust in relativistic shocks (see, e.g., ZM06). We separately reconstruct the components of the relative 3-velocity, $\tilde{v}^i \equiv \tilde{u}^i/\gamma$, and γ . We then multiply the interpolated value of \tilde{v}^i by that of γ to get the reconstructed value of the relative 4-velocity.

We perform the averaging and de-averaging reconstructions component-by-component on the conserved quantities and fluxes. To make the evolution of our scheme failsafe, especially since an arbitrary interpolation of the conserved quantities and fluxes can lead to an unphysical state, we implement some features that are more likely to give a physical state (see Appendix A8).

4.2 Multi-dimensional reconstruction

To perform reconstructions in more than one dimension, we use the dimension by dimension approach. It uses one-dimensional reconstructions, described in the rest of this section, as building blocks for a multidimensional reconstruction. This method was found to be faster than a genuine multidimensional reconstruction and have a similar accuracy (Shi et al. 2002). The generalization of the

cell centre to interface reconstruction to multi dimensions is straightforward: we perform one-dimensional cell centre to interface reconstructions independently for each dimension. In several dimensions the average to centre and centre to average reconstructions are performed by applying one-dimensional reconstructions sequentially dimension by dimension (Shu 1997). We symmetrize this procedure by averaging over all possible permutations of the sequences for which the one-dimensional reconstruction can be applied (see also Aloy et al. 1999). This allows us to maintain the symmetry of the reconstruction and is our default choice for this paper. In particular, we maintain *exact* symmetry for two-dimensional problems.² For multidimensional problems that do not require the preservation of symmetry, computational efficiency can be improved by using Strang-type splitting. Without loss of accuracy, we could do this for the two-dimensional problems described in sections 5.21, 5.22, and 5.23. However, we use the same settings throughout the paper for the sake of showing the ability to use WHAM with one single set of parameters for a wide range of problems.

4.3 One-dimensional reconstruction

Consider a one-dimensional grid along the x axis consisting of grid cells $\Delta_i \equiv (x_{i-1/2}, x_{i+1/2})$ with cell centres located at points $x_i = x_0 + h i$, where h is the grid cell size. Godunov-type schemes require the conversion of quantities from one type of discretised representation on the grid to another: e.g., from cell-centred values of density ρ_i to cell-interface values $\rho_{i+1/2}$.

Since in this example the particular dependence of $\rho(x)$ is unknown (only known through its discretisation at cell centres ρ_i), in order to get the discretisation of density at cell interfaces, we first reconstruct a smooth density profile inside each of the grid cells. For this, we use the values of ρ_i in several grid cells around the grid cell in which the reconstruction is being performed; this set of grid cells is called the *stencil*. Then, we combine the reconstructed profiles inside each of the grid cells to obtain the global reconstruction $\tilde{\rho}(x)$. Now we can easily obtain the cell-interface (or any other) representation of density by evaluating $\tilde{\rho}(x)$ at the locations of the interfaces (or any other locations). By construction, the global reconstruction is smooth inside each grid cell and is in general discontinuous at cell interfaces. For this reason, we adopt a convention by which $\tilde{\rho}_{i+1/2} \equiv \tilde{\rho}(x_{i+1/2-0})$ and $\tilde{\rho}_{i-1/2} \equiv \tilde{\rho}(x_{i-1/2+0})$, i.e. the one-half in the indices is replaced with a value infinitesimally smaller than one-half.

Within piecewise smooth functions the reconstruction is not unique, and the goal is to find such a reconstruction out of many possible ones that would give high order of convergence in smooth regions and lead to minimal spurious oscillations near discontinuities.

² The internal registers are often higher precision than the precision of variables (e.g., 80-bit for Intel 32-bit machines vs. 64-bit for double precision variables) so that one must use a compiler option (e.g., -pc64 for Intel compilers) to disable the use of such internal precision. These compiler options are only used on those parts of the code that involve operations with multiple points at the same time. In the case of Intel compilers, one must use the -mp compiler option as well in order to restrict the optimizations to maintain the order of operations.

¹ ‘IFV’ stands for Inconsistent Finite Volume, and ‘IS’ stands for Inconsistent Source.

Along with the cell centre to interface reconstruction considered above, this paper makes use of other reconstruction types that can be formulated similarly. Section 4.6 below gives more detail.

In the regions where the flow is smooth the reconstruction should be of high order to ensure fast convergence to the actual solution when the grid is refined. However, *next to* a kink or a shock, the scheme should avoid using stencils that contain this non-smooth feature and should instead use stencils that reside entirely within the smooth regions of the flow: failure to do so would lead to spurious oscillations.

4.4 Overview of existing algorithms

In this section we review some existing methods for reconstruction. The goal of such methods is to provide higher-order accuracy than a piecewise constant reconstruction, while avoiding spurious oscillations in the presence of discontinuities.

Common existing approaches are the following: MINMOD, Monotonized Central (MC), van Leer, Piecewise Parabolic Method (PPM), Essentially Non-Oscillatory (ENO) and Weighted Essentially Non-Oscillatory (WENO) schemes. Throughout the paper, the order of the schemes/reconstructions refers to the order of their truncation error.

In general, MINMOD, MC, and van Leer schemes are second order in smooth regions of the flow. Parts of the reconstruction algorithm used in Piecewise Parabolic Method (PPM) are 4th order. PPM is a computationally fast reconstruction method and is able to resolve contact discontinuities well (Colella & Woodward 1984; Gardiner & Stone 2005; Mignone et al. 2005). The standard PPM scheme is dimensionally split, resulting in second order accuracy even for smooth monotonic flows. Also, when used for the reconstruction of primitive quantities it is in general second order in smooth monotonic regions because it does not account for the difference between point and average values of conserved quantities (Blondin & Lufkin 1993, ZM06).

The schemes in the above paragraph provide a total variation diminishing (TVD) reconstruction, i.e. they do not increase a measure of the number and magnitude of function extrema with time (Harten 1983). This produces non-oscillatory and robust solutions. However, being TVD also means these reconstructions satisfy the maximum principle that the reconstructed value at an interface lies in between the values at the two neighboring cell centres. Therefore, near extrema, where the derivative changes sign, the so-called *clipping* phenomenon may occur: extrema are flattened thereby increasing the truncation error of the scheme near smooth extrema and lowering the order of the scheme there to first order (Harten et al. 1987; Jiang & Tadmor 1998).

Essentially Non-Oscillatory schemes provide a uniformly high order accurate reconstruction, do not suffer from the clipping phenomenon, provide a total variation bounded reconstruction (TVB), and give robust solutions for flows with discontinuities (Harten et al. 1987). They choose the smoothest stencil out of a set of possible stencils of a fixed length. The weakness of this approach is that one needs to choose *one* stencil even if there are several equivalently smooth ones, e.g., when the function is a constant. There-

fore, unless certain measures are taken (see, e.g., Shu 1997), numerical noise, which is always present, may start influencing the stencil choice procedure. This is referred to as *free stencil adaptation* and may lead to the numerical noise being amplified. Further, these schemes require a computationally intensive eigenvector decomposition to minimize the Gibbs phenomenon near shocks.

Convex Essentially Non-Oscillatory schemes (CENO, Liu & Osher 1998) are similar to ENO schemes in that they choose one out of the possible stencils for performing the reconstruction, but include a mechanism for reducing the stencil size in discontinuities. The latter feature allows these algorithms to avoid the use of expensive eigenvector decomposition, making it easier to apply them to general relativistic problems, as was done by Anderson et al. (2006) and Mizuno et al. (2006), who achieve third order convergence in smooth flows. However, the CENO method can give non-smooth results since the stencil choice may change discretely between adjacent grid cells.

Weighted Essentially Non-Oscillatory schemes (WENO) are designed to provide smooth numerical flux and do not suffer from the free stencil adaptation problem (Shu 1997). Instead of using only the smoothest stencil, they take a linear combination with coefficients, called *weights*, of all possible stencils of a given size. The weights in the linear combination add up to unity and are distributed in such a way that stencils that contain discontinuities get extremely small weight. Further, the weights are designed in such a way that when the function is smooth in all stencils, the weights become close to the optimal ones so that the resulting linear combination of the stencils gives a higher order approximation – the same order as the one that the larger, combined, stencil would give. WENO-based schemes are advantageous because they are able to both capture shocks and accurately resolve complex smooth flow structure. Several groups have had success in developing WENO-based schemes in application to relativistic astrophysics (Rahman & Moore 2005; Zhang & MacFadyen 2006) and cosmology (Feng et al. 2004; Qiu et al. 2006). The high accuracy of WENO schemes enables them to be used in studies of high Mach number astrophysical flows (Ha et al. 2005).

4.5 Weighted essentially non-oscillatory schemes

Because of the advantages of the WENO method, we have implemented this scheme in our code. Consider the one-dimensional grid along the x axis that was defined in section 4.3. Its cell centres are located at points $x_i = x_0 + h i$, where h is the grid cell size. The right interface of the i th cell is located at $x_{i+1/2} = x_0 + h(i + 1/2 - 0)$.

We first consider the *cell centre to right interface* reconstruction. Given the values of a piecewise smooth function $v(x)$ at the cell centres, $v_i = v(x_i)$, we aim to reconstruct the function value $v_{i+1/2}$ at the interface $x = x_{i+1/2}$. Consider k candidate stencils, each of length k :

$$s_r(i) = \{x_{i-r}, \dots, x_{i-r+k-1}\}, \quad r = 0, \dots, k-1. \quad (17)$$

Each of these stencils produces its own reconstruction of the

function value $v_{i+1/2}$ (Shu 1997):

$$v_{i+1/2}^{(s_r)} = \sum_{j=0}^{k-1} c_{rj} v_{i-r+j}, \quad r = 0, \dots, k-1. \quad (18)$$

with truncation error of $\mathcal{O}(h^k)$ (see Appendix A2 for numerical values of the coefficients c_{ij}).

Within the WENO scheme, the reconstructed value of $v(x_{i+1/2})$ is written as a linear combination of the reconstructions due to each of the stencils s_r :

$$v_{i+1/2} = \sum_{r=0}^{k-1} \omega_r v_{i+1/2}^{(s_r)}; \quad (19)$$

the weights ω_r are all nonnegative and sum up to unity. The heart of the scheme is the proper choice of these weights.

In the regions where $v(x)$ is smooth, we define a WENO- n scheme as one that delivers a reconstruction of order $n = 2k - 1$, the same order as that of the reconstruction $v_{i+1/2}^{(S)}$ due to the combined stencil $S = \bigcup_{r=0}^{k-1} s_r(i)$:

$$v_{i+1/2}^{(S)} = \sum_{j=i-k+1}^{i+k-1} c_j v_j, \quad (20)$$

with truncation error $\mathcal{O}(h^n)$. Usually, such constants d_r can be found that for $\omega_r = d_r$ the reconstructions given by equations (19) and (20) are exactly equivalent, i.e. $v_{i+1/2} \equiv v_{i+1/2}^{(S)}$. We refer to the constants d_r as the *optimal weights*; their values are given in Appendix A2.

However, the exact identity is a too strict restriction on the weights. In fact, the weights ω_r can deviate from the optimal weights d_r in smooth regions and still produce a truncation error of the same order: by (19), requiring that

$$\omega_r = d_r + \mathcal{O}(h^{k-1}), \quad r = 0, \dots, k-1, \quad (21)$$

guarantees the same order of truncation error (cf. formula (2.57) in Shu 1997). Equation (21) is the requirement on the weights in regions where $v(x)$ is smooth. When there are shocks, the stencils that contain discontinuities should be given extremely small weight.

4.6 Types of reconstruction

We have just outlined the cell centre to right interface reconstruction. It inputs a set of point values at the centres of grid cells, $\{v_i\}$, and outputs a set of values at the grid cell interfaces, $\{v_{i+1/2}\}$.

Analogously, we introduce the following types of reconstruction: centre to left interface, $\{v_i\} \rightarrow \{v_{i-1/2}\}$, centre to average, $\{v_i\} \rightarrow \{\langle v \rangle_i\}$, and average to centre, $\{\langle v \rangle_i\} \rightarrow \{v_i\}$. Here $\langle v \rangle_i = h^{-1} \int_{\Delta_i} v(x) dx$, $\Delta_i \equiv (x_{i-1/2}, x_{i+1/2})$, is the average of $v(x)$ over the i th grid cell. Apart from the trivial change in the input and/or output notation,³ formulae (18) – (21) hold for all these types of reconstruction as well. Appendix A2 gives the values of the coefficients c_{ij} and d_r for each reconstruction type used by the scheme.

³ For instance, for the centre to average reconstruction one uses $\langle v \rangle_i$ for the symbol of the output quantity instead of $v_{i+1/2}$.

4.7 WENO prescription for weights

In the WENO scheme (Jiang & Shu 1996; Shu 1997), the weights are computed based on *smoothness indicators*, β_r . These indicators give a measure of the variation of $p_r(x)$ – the reconstruction polynomial due to the stencil $s_r(i)$ – within the grid cell Δ_i . The smoothness indicators are defined as:

$$\beta_r = \frac{1}{h} \int_{x_{i-1/2}}^{x_{i+1/2}} \left[\sum_{n=1}^{k-1} \left(\frac{\partial^n p_r(x)}{\partial x^n} h^n \right)^2 \right] dx, \quad (22)$$

where the factors of h are included to remove any grid cell size dependence of β_r . According to the definition (22), a smoothness indicator is the average over the cell of interest of the sum of the squares of all derivatives of the interpolating polynomial. Therefore, a smoothness indicator measures how deviant from a constant the reconstruction is. The smaller the smoothness indicator, the flatter the reconstructed profile, i.e. the smaller the change of the interpolating polynomial $p_r(x)$ over the cell of interest. The smoothness indicators defined by (22) are specified for WENO-5 by equation (A18) in appendix A4.

Jiang & Shu (1996) define the unnormalized weights in the following way:

$$\tilde{\omega}_r = \frac{d_r}{(\epsilon + \beta_r)^2}, \quad (23)$$

which, when normalized, become:

$$\omega_r = \tilde{\omega}_r / \Omega, \quad (24)$$

where $\Omega = \sum_{r=0}^{k-1} \tilde{\omega}_r$ is the sum of unnormalized weights and ϵ is a small positive parameter.

The ϵ parameter in (23) is introduced to avoid division by zero. Values used by workers vary from 10^{-4} – 10^{-6} (Jiang & Shu 1996; Shu 1997; Titarev & Toro 2004; Zhang & MacFadyen 2006) to 10^{-10} (Balsara & Shu 2000). However, setting this parameter in any problem independent way introduces an artificial scale into the problem since discontinuities smaller than this scale are considered to be part of the smooth flow. It is therefore preferable to dynamically choose ϵ such that it is large enough to avoid the triggering of the scheme on machine level noise and yet small enough not to influence the weights calculation in other cases (see, however, Jiang & Shu 1996). We describe the procedure we use in Appendix A3.

Note that for centre to average and average to centre reconstructions some of the optimal weights become negative, and using negative weights can lead to an instability (Shi et al. 2002). This problem can be avoided by a simple technique that keeps the sum of the absolute values of the weights bounded (Shi et al. 2002). We use this technique for both average to centre and centre to average reconstructions.

Equation (24) assigns larger weights to the stencils with smaller smoothness indicators, i.e., with flatter reconstruction profiles and smaller degree of oscillation. These weights become extremely small for a stencil that contains a discontinuity; this is referred to as *adaptive stencil choice* and provides the nonoscillatory property of the scheme. At the same time, weights (24) are designed to be close to the optimal weights according to (21) for a smooth flow locally well-approximated by a parabola. Therefore, for such flows,

the WENO-5 scheme is fifth order in space. However, there are other flows for which the scheme becomes third order.

4.8 Convergence properties of WENO-type schemes in smooth flows

Preserving a high order interpolation near extrema and at the same time maintaining the nonoscillatory property of the solution is a challenging problem (Harten et al. 1987). For instance, all schemes that satisfy the monotonicity constraint reduce to first order near extrema.

WENO-5 reconstruction is very appealing in that it maintains high order near extrema. For a common type of extremum, one with a nonvanishing second derivative, it is claimed to be fifth order by Jiang & Shu (1996); Shu (1997). However, we have found that in general the WENO-5 scheme becomes fourth order near such extrema. Further, for a smooth flow whose Taylor series expansion is dominated by third or higher order terms, the WENO-5 scheme reduces to third order. Appendix A4 discusses the convergence properties of the WENO-5 scheme in more detail and gives expressions for the smoothness indicators. To help minimize the excessive reduction of order by the standard WENO-5 scheme, our scheme uses the full stencil (20) in regions where this stencil gives monotonic values for the function and all of its derivatives (see Appendix A5).

One can construct WENO-type schemes of an arbitrarily high order (e.g. seventh, ninth, etc.) that deliver an even higher order when the lower-order derivatives vanish. Such schemes provide a much better resolution of contact discontinuities and smooth features of the flow than their lower-order counterparts, given the same grid cell size (Latini et al. 2007). However, they also require more computational effort (see, e.g., Qiu & Shu 2002). Appendix A6 proves some properties of higher order WENO-type schemes, discusses their benefits, and points out their limitations for handling critical points in smooth flows.

The use of WENO weights alone is known to be insufficient in avoiding spurious oscillations near discontinuities, and a known remedy is to use eigenvector decomposition. In the next section, we discuss our alternative approach that does not require computing the eigenvectors.

4.9 Oscillation-free reconstruction

Interpolating the primitive, conserved, or any other arbitrary quantities can in general lead to spurious oscillations. Such oscillations can be introduced because the interpolations allow arbitrary mixing between different eigenmodes.

One can avoid significant spurious oscillations by reconstructing the so-called wavestrengths, the wave amplitudes in the local characteristic fields (Qiu & Shu 2002). We generically refer to this procedure as the eigenvector decomposition approach. Interpolating each wavestrength individually in most cases leads to only small mixing between different eigenmodes (Harten et al. 1987). There are several types of reconstructions based on this idea: characteristic-wise reconstruction, field-by-field reconstruction, etc. (Harten et al. 1987; Shu & Osher 1988, 1989; Shu 1997). All are computationally intensive and require sophisticated coding that becomes complicated for the GRMHD case.

We adopt an alternative approach that involves locally reducing the order of the scheme near discontinuities (Colella & Woodward 1984; Liu & Osher 1998; Mignone et al. 2005). The Riemann solver is fed interface values that are close to first order near shocks. This procedure reduces the mixing between different eigenmodes and makes the scheme more robust. Further, since this approach does not require the computation of any eigenvectors, it can be used to solve weakly hyperbolic systems. It is computationally more efficient than eigenvector decomposition, and is easier to implement (Liu & Osher 1998). See Appendix A7 for a discussion.

5 NUMERICAL TESTS

We have confirmed the accuracy and robustness of our code by running an extensive series of tests. We begin the discussion with four tests that show the importance of distinguishing between the average and point values of conserved quantities. We then discuss a number of standard tests in the literature. Our scheme successfully evolves all nonrelativistic hydrodynamic tests from Liska & Wendroff (2003a, LW03) and all chosen tests from Zhang & MacFadyen (2006, ZM06), but we only discuss those tests we found to be most challenging. Finally, we discuss some general relativistic tests from Gammie et al. (2003).

Table 1 provides detailed information on some of the one-dimensional test problems. Unless otherwise indicated, we use the exact Riemann solvers by Toro (1997) and Giacomazzo & Rezzolla (2006) to obtain the exact solutions for nonrelativistic and relativistic one-dimensional Riemann test problems, respectively.

For nonrelativistic problems we set the value of the speed of light in the scheme to 10^{10} so that any velocity on the order of unity is then nonrelativistic to machine accuracy (i.e. $\gamma - 1 = 0$). All problems use the ideal gas equation of state, $p_g = (\Gamma - 1)u_g$, where Γ is the adiabatic gas index.

For all tests, we use a *constant* set of numerical parameters that control the behavior of the scheme. This is as opposed to many other works that fine-tune their numerical parameters in order to make some tests work. The fact that we are able to run all the tests with a single set of parameters proves the robustness of our method as a single scheme to study a vast array of problems. We use WHAM scheme with a Courant factor of 0.5 and the approximate HLL Riemann solver for all tests.

5.1 Smooth high Mach number flow: Hubble-type flow

This is a simple high Mach number flow problem that tests the ability of a numerical scheme to handle flows with disparate energy scales. The problem is defined in section 3.2. For the test described here the flow parameters are set as follows:

$$\rho_0 = 1, \quad (25)$$

$$v'_0 = 1, \quad (26)$$

$$u_0 = 4 \times 10^{-8}, \quad (27)$$

Table 1. Parameter values selected for the one-dimensional nonrelativistic Riemann problems, shock - entropy wave interaction problem, and relativistic Riemann problems. All problems are run on the interval $(0, 1)$, except the shock - entropy wave interaction problem on $(-5, 5)$, Sod's problem on $(-1.5, 1.5)$, and moving Sod's problem on $(-1.5, 25.5)$. The initial position of the discontinuity is located at $x = x_0$, the tests are run until the final time t_F , with gas adiabatic index of Γ , with N grid cells. Here ρ is the density, v_x and v_y the 3-velocity components, and p_g the pressure. 'L' denotes the left state and 'R' the right state.

Test	ρ_L	$v_{x,L}$	$v_{y,L}$	$p_{g,L}$	ρ_R	$v_{x,R}$	$v_{y,R}$	$p_{g,R}$	Γ	x_0	t_F	N	Sec.
Sod	1	0	0	1	0.2	0	0	0.01	5/3	0.0	0.77	150	5.2
Moving Sod	1	28.87	0	1	0.2	28.87	0	0.01	5/3	0.0	0.77	1350	5.2
Noh	1	1	0	0	1	-1	0	0	5/3	0.5	1	100	5.5
Moving contact	1.4	0.1	0	1	1	0	0.1	1	1.4	0.5	2	100	5.6
Test 4	5.99924	19.5975	0	460.894	5.99242	-6.19633	0	46.095	1.4	0.4	0.035	200	5.7
Shock - entropy	3.857143	2.629369	0	10.33333	$1 + 0.2 \sin(5x)$	0	0	1	1.4	-4	1.8	400	5.8
Rel. problem 1	10.0	0	0	13.33	1.0	0	0	10^{-8}	5/3	0.5	0.4	400	5.14
Rel. problem 2	1.0	0	0	1000	1.0	0	0	10^{-2}	5/3	0.5	0.4	400	5.15
Rel. problem 3	1.0	0.9	0	1	1.0	0	0	10	4/3	0.5	0.4	400	5.16
Rel. problem 4	1.0	0	0	1000	1.0	0	0.99	10^{-2}	5/3	0.5	0.4	400	5.17
Rel. problem 5	1.0	0	0.9	1000	1.0	0	0.9	10^{-2}	5/3	0.5	0.6	400	5.18
Rel. problem 6	1.0	$1 - 10^{-10}$	0	0.001	(uses reflecting boundary at $x = 1$)				4/3	1.0	2	100	5.19

with $\Gamma = 1.4$. We employ a resolution of 64 cells on the interval $(-1, 1)$, so that the Mach number varies from $M_{\min} \approx 104.4$ to $M_{\max} \approx 6577.1$ at the grid cell centres. For the values in the boundary cells we use linearly extrapolated values of the primitive quantities.

The Hubble-type flow problem illustrates how crucial it is to account for the difference between cell averaged and cell centred conserved quantities in high Mach number flows. Table 2 shows the relative L_1 -error in the internal energy and other quantities at the characteristic time of evolution, $t_F = 1$, for the WHAM, WENO-IFV, HARM,⁴ and Athena⁵ schemes. We define the absolute L_1 -error norm of any quantity u as

$$\Delta_A u \equiv (\Delta u)_{L_1} = \sum_j |u_j^{\text{numerical}} - u_j^{\text{exact}}| / N, \quad (28)$$

where N is the number of elements, and the relative L_1 -error norm as

$$\Delta_R u \equiv (\Delta u / u_{\max})_{L_1} = \Delta_A u / \max_i |u_i^{\text{exact}}|. \quad (29)$$

Since WHAM performs the proper conversion between cell averaged and cell centred conserved quantities before the reconstruction step, it is 4th order accurate in time and gets the final distribution of internal energy with a relative L_1 -error of only 5% at the default resolution of $N = 64$.⁶

In contrast, the WENO-IFV, HARM, and Athena

⁴ The HARM scheme converges at second order in space and time and does not account for the difference between cell averaged and cell centred values of conserved quantities, see Gammie et al. (2003).

⁵ We use Athena 2.0 (Stone 2006) with third order spatial interpolation and the Roe solver. We use a Courant factor of 0.5. For setting the values in the boundary grid cells we use quadratically extrapolated values of conserved quantities.

⁶ 4th order accuracy in time at one time step implies an error term of $\mathcal{O}(\Delta t^5)$. Therefore, the error due to evolution from $t = 0$ to $t = t_F$ is $n \times \mathcal{O}(\Delta t^5) \sim \mathcal{O}(\Delta t^4) \sim \mathcal{O}(C^4)$, where $n = t_F / \Delta t$ is the number of time steps to reach the final time t_F and $C = \mathcal{O}(\Delta t)$ is the Courant factor.

Table 2. Relative L_1 -error and convergence order in internal energy at the final time $t_F = 1$ for the Hubble-type flow problem (section 5.1). The Courant factor is C , and the resolution is N . The WENO-IFV, HARM (Gammie et al. 2003), and Athena (Stone 2006) schemes converge at second order in space and at zeroth order in time in agreement with equation (13). One has to increase the resolution by a factor of more than 100 to match the performance of the WHAM scheme. WHAM converges at 4th order in space and time, see the note after equation (16).

Scheme	C	N	$\Delta_R u_g$	Order
WHAM	0.5	64	5.2e-2	
	0.5	128	4.3e-3	3.6
	0.5	256	3.1e-4	3.8
	0.5	512	2.1e-5	3.9
	0.5	1024	1.4e-6	3.9
	0.05	64	5.2e-6	4.0
WENO-IFV	0.5	64	1278	
	0.5	640	12.78	2.0
	0.5	6400	12.78e-2	2.0
	0.5	9600	5.7e-2	2.0
	0.5	25600	0.8e-2	2.0
	0.05	64	1278	0.0
HARM	0.5	64	773.3	
	0.5	640	7.8	2.0
	0.5	6400	7.8e-2	2.0
	0.5	7680	5.4e-2	2.0
	0.5	9600	3.4e-2	2.0
	0.05	64	1273	-0.2
Athena	0.5	64	2527	
	0.5	640	30.43	1.9
	0.5	6400	0.14	2.3
	0.5	12000	4.2e-2	1.9
	0.05	64	2459	0.01

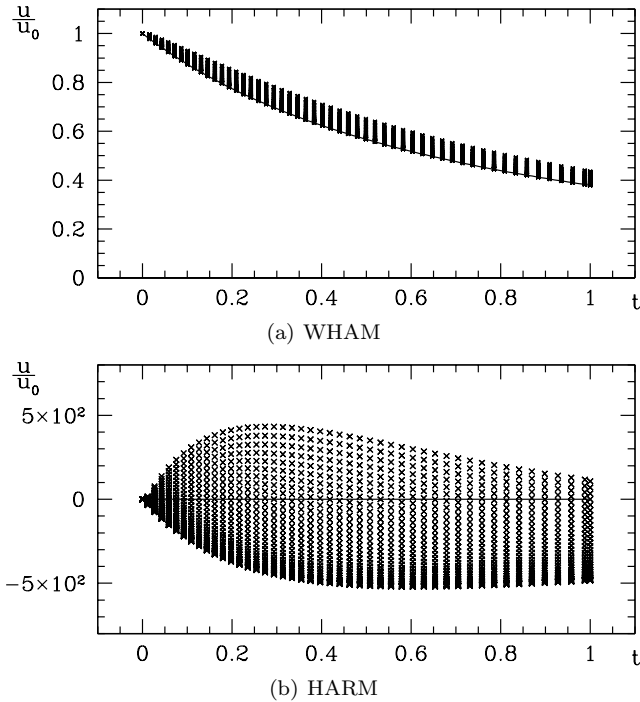


Figure 3. Analytical and numerical solutions for the Hubble-type flow problem, section 5.1, at a resolution of $N = 64$. At each time step a scatter plot of dimensionless values of internal energy is shown for WHAM (a) and HARM (b). The analytical solution (12) for internal energy is shown with a solid line on each panel. Note that on panel (b) the analytic solution is compressed into a horizontal line because the vertical scale has been changed by a factor of about 1000. WHAM accurately captures the dependence of the internal energy in this highly supersonic flow, while other schemes (including HARM and Athena) that do not differentiate between the average and point values of conserved quantities makes a large error in internal energy.

codes, which do not perform the average to centre conversion, produce large errors. In fact, they obtain a negative value of the internal energy already after the first time step.⁷ When the internal energy is negative, for the WENO-IFV and HARM schemes we set the sound speed to 0; for Athena, we use its default settings.

Figure 3 visualizes the time dependence of the internal energy for the WHAM and HARM schemes. The solution for internal energy given by WHAM deviates only slightly from the analytic solution. The internal energy given by HARM becomes negative after the first time step and is very nonuniform in space. Any scheme (including HARM and Athena) that does not differentiate between the average and point values of conserved quantities will make a similar error. This error in the internal energy is second order in space, with a large coefficient proportional to the square of the Mach number (see eq. 13). This error does not decrease if the time step is decreased. For these schemes one has to use a resolution more than 100 times larger than the default one to match the accuracy of the WHAM scheme at the default

⁷ We note that a first order Godunov scheme with an approximate HLL Riemann solver produces inaccurate but physical values of the internal energy.

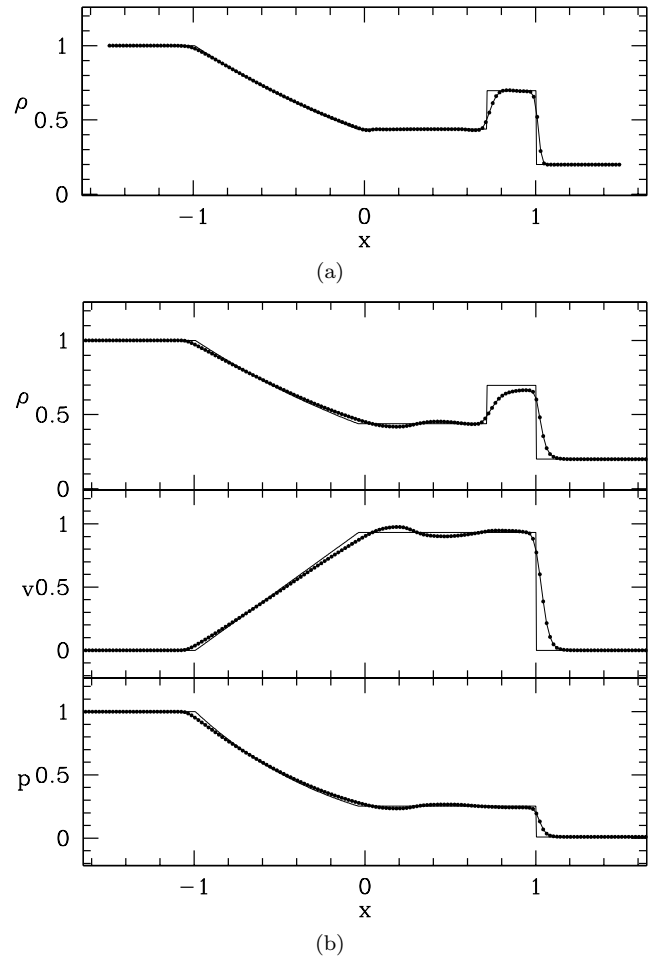


Figure 4. Panel (a) shows the standard Sod's problem. Panel (b) shows the 'moving Sod's problem' with the pre-shock state moving supersonically through the grid at a Mach number of 100. The numerical solution by the WHAM scheme is shown with connected dots and the analytic solution is shown with a solid line. For the lower panel (b) the x -coordinate has been remapped to correspond to the same range as in panel (a). WHAM is able to accurately treat shocks when both the pre-shock and post-shock regions are moving supersonically.

resolution (see table 2). In other words, for high Mach number problems, high order schemes are much more effective than lower order ones.

5.2 Discontinuous high Mach number flow: Sod's shock tube

In this section we consider two versions of Sod's problem (Trac & Pen 2004). The first 'stationary' version is a standard, simple shock tube problem, a variation of the original problem by Sod (1978). Table 1 shows the initial conditions for this problem and figure 4(a) shows the density distribution given by the WHAM scheme overplotted on the exact solution at the final time.

The second 'moving' version is the 'stationary' problem boosted to a supersonic speed such that the pre-shock Mach number of the initial right state of the problem is equal to 100. This verifies the code's ability to handle shocks with

both pre-shocked and post-shocked gas moving supersonically with respect to the grid. Godunov-type schemes that operate on a fixed Eulerian grid are claimed to have serious difficulties, e.g., producing the wrong height of the shock and generating spurious post-shock oscillations (Trac & Pen 2004).

In studying the ‘moving’ version of Sod’s problem with WHAM, we keep the same grid cell spacing and the final time as in the ‘stationary’ version but extend the grid so that the wave structure does not go off the grid until the final time of the test (see table 1). We have performed this problem with both the WHAM scheme, see figure 4(b), and with HARM (Gammie et al. 2003). We find that neither scheme shows the suggested violent post-shock oscillations claimed by Trac & Pen. It could be that their numerical scheme has difficulties because it reconstructs the conserved quantities, not primitive quantities. The lower order HARM scheme gets an incorrect height of the shock for the ‘moving’ problem (and produces the correct shock height in the ‘stationary’ version of the problem). This phenomenon also occurs with the Eulerian scheme of Trac & Pen (2004).

Without the moving grid technique of Trac & Pen (2004), WHAM is able to obtain a comparable resolution of the contact discontinuity and value of the shock height. This shows that accounting for the difference between the point and average values of conserved quantities is an alternative to the moving grid scheme of Trac & Pen (2004). WHAM converges uniformly at first order for this test.

5.3 One-dimensional hydrodynamic caustics

In this problem (see figure 5) a highly supersonic smooth flow steepens into a pair of shocks posing challenges for numerical schemes: the ability to accurately evolve a smooth high Mach number flow and handle its interaction with strong shocks. Initially the density and the pressure are uniform, $\rho = 1$ and $p = 10^{-10}$, and the velocity is a sine wave, $v(x) = (2\pi)^{-1} \sin(2\pi x)$. This corresponds to Mach number reaching 1.2×10^4 and the internal energy accounting only for about 10^{-8} of the kinetic energy. We run the problem on an interval $(0, 1)$ until time $t_F = 3$ with periodic boundary conditions and we use a resolution of 128 grid cells as chosen by Ryu et al. (1993).

For this problem Ryu et al. (1993) find that schemes evolving the total energy make unacceptably large errors in the internal energy even at very high resolutions. Ryu et al. (1993) therefore argue for the ‘dual-energy formalism’ in which one switches to evolving the entropy equation in the high Mach number regions of the flow. Although such an approach does not suffer from the high Mach number problem in smooth supersonic flows, it cannot account for dissipation in weak shocks (see section 1).

WHAM correctly captures shocks in highly supersonic flows (see the previous section) and for smooth flows quickly converges to the correct solution as the resolution is increased. Figure 5 shows WHAM getting the final distribution of pressure in the high Mach number region within a factor of 3 from the converged solution. This is 4 orders of magnitude better than the energy-conserving scheme of Ryu et al. (1993). The shock is always resolved with about four points. Using a resolution of 180 and a Courant factor of 0.2 gives a pre-shock pressure error of only 10%. With

a resolution of 256 and the standard Courant factor of 0.5, the error is reduced by a factor of $10 \approx 2^{3.5}$ to 25%, i.e. our scheme converges in pointwise sense at 3.5th order in the pre-shock region. HARM or Athena, which are strictly second order in supersonic flows and do not improve their error for smaller Courant factors, obtain an error $\sim 25\%$ only at a resolution of $\sim 45,000$ grid cells.

5.4 Linear wave advection

To verify the order of convergence of WHAM, we perform the advection of smooth sound and density waves in Cartesian coordinates in two dimensions. This verifies the order and accuracy of the multidimensional reconstruction and of the Runge-Kutta time stepping.

We have set up this test in the same way as in the Athena code (Stone 2006). For both the density and sound wave advection problems, we choose a wave with a wave vector $\mathbf{k} = (k_x, k_y) = (2\pi/\sin\alpha, 2\pi/\cos\alpha)$ directed at an angle $\alpha = \tan^{-1}(2) \approx 64.4$ degrees w.r.t. the x -axis. We use a computational box of size $(0, \sin\alpha) \times (0, \cos\alpha)$ such that periodic boundary conditions can be applied. The number of grid cells in the x -direction is twice that in the y -direction so that each grid cell is a square even though the computational box is a rectangle. Therefore the wave does not travel along the diagonal of grid cells guaranteeing that the test is truly multidimensional.

We use an equation of state with $\Gamma = 5/3$ and choose a uniform background state with a unit density $\rho_0 = 1$ and a unit sound speed $c_{s,0} = 1$, which corresponds to the background internal energy $u_0 = 0.9$. For the sound wave test we choose the background velocity to be zero ($\mathbf{v}_0 = \mathbf{0}$) and for the density wave test we choose the background velocity to be unity along the direction of the wave vector ($\mathbf{v}_0 = \mathbf{k}/|\mathbf{k}|$). We run both tests for one temporal period T of the wave, i.e. until $t_F = T = 0.4$. Relative perturbations for the sound wave include perturbations in density, velocity, and internal energy,

$$\begin{pmatrix} \delta\rho/\rho_0 \\ \delta\mathbf{v}/c_{s,0} \\ \delta u/u_0 \end{pmatrix} = A \cos(\mathbf{k} \cdot \mathbf{r}) \begin{pmatrix} 1 \\ \mathbf{k}/|\mathbf{k}| \\ \Gamma \end{pmatrix}, \quad (30)$$

whereas for the density wave the perturbations are only in density,

$$\begin{pmatrix} \delta\rho/\rho_0 \\ \delta\mathbf{v}/c_{s,0} \\ \delta u/u_0 \end{pmatrix} = A \cos(\mathbf{k} \cdot \mathbf{r}) \begin{pmatrix} 1 \\ 0 \\ 0 \end{pmatrix}. \quad (31)$$

We choose the relative magnitude A of the perturbation such that nonlinear wave effects for the sound wave at the final time lead to relative nonlinear corrections δ_{NL} to the solution on the order of the numerical precision for our machine, $\delta_{NL} \sim A^2 t_F / T = \epsilon_{\text{machine}} \approx 10^{-15}$, so we set $A = 3.2 \times 10^{-8}$.

We perform the calculations at different resolutions. Table 3 shows that the WHAM scheme indeed converges at fifth order. For comparison, we have also run the density and sound wave tests using the WENO-IFV scheme, HARM, and Athena. These three schemes converge only at second order despite the cell centre to interface reconstruction used in the WENO-IFV scheme being fifth order. This shows that not making a distinction between the average and point values

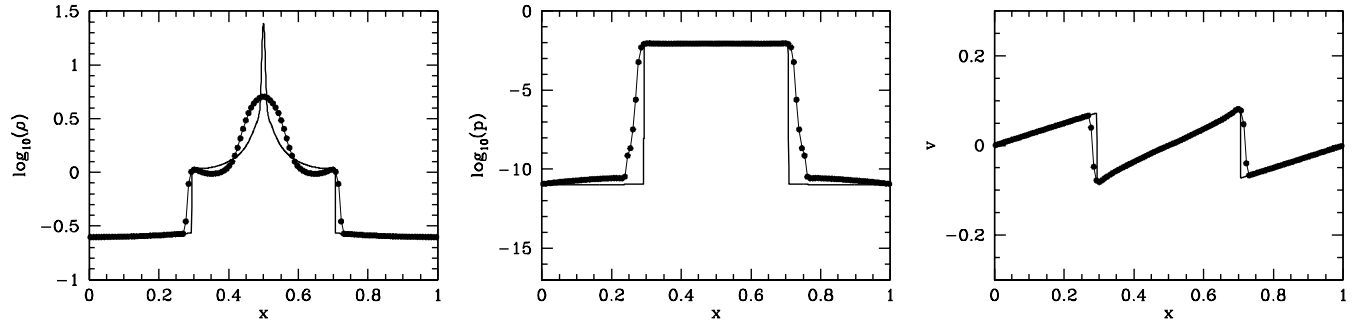


Figure 5. Density, pressure, and velocity for the one-dimensional hydrodynamic caustics problem at time $t_F = 3$. Connected dots show the result of WHAM at the resolution of $N = 128$ grid cells with the standard Courant factor of $C = 0.5$ and the solid line shows the converged solution obtained with $N = 2048$ grid cells. With $N = 128$ and $C = 0.5$, WHAM reproduces the low pressure pre-shock region with an error of 250% that is several orders of magnitude smaller than with the energy conserving scheme of Ryu et al. (1993). With $N = 180$ and $C = 0.2$, the pre-shock pressure error is only 10% with WHAM, and with $N = 256$ and $C = 0.5$ the error is 25%. Highly accurate, higher-order energy conserving schemes like WHAM are capable of obtaining acceptable solutions for extremely high Mach number flows without resorting to the dual-energy formalism, recommended by Ryu et al. (1993)

Table 3. Relative L_1 -error in density, $\Delta_R \rho$, and the order of convergence (base 2 logarithm of the error) of WHAM, WENO-IFV and HARM schemes for the two-dimensional density and sound wave problems (section 5.4). The WHAM scheme converges to the analytic solution at fifth order for both problems, while the WENO-IFV scheme and the HARM scheme converge only at second order.

Resolution	16×8	32×16	64×32	128×64
Entropy wave				
WHAM	3.9e-09	9.2e-11	2.6e-12	8.0e-14
Order	—	5.5	5.2	5.0
WENO-IFV	5.5e-09	7.1e-10	1.7e-10	4.4e-11
Order	—	3.0	2.0	2.0
HARM	7.7e-09	1.6e-09	5.9e-10	1.7e-10
Order	—	2.2	1.5	1.7
Athena	2.9e-09	1.1e-09	2.7e-10	6.9e-11
Order	—	1.4	2.1	2.0
Sound wave				
WHAM	4.0e-09	9.2e-11	2.6e-12	8.0e-14
Order	—	5.4	5.1	5.0
WENO-IFV	5.5e-09	7.1e-10	1.7e-10	4.4e-11
Order	—	3.0	2.0	2.0
HARM	7.9e-09	1.8e-09	6.3e-10	1.9e-10
Order	—	2.2	1.5	1.8
Athena	2.5e-09	6.5e-10	1.8e-10	4.2e-11
Order	—	1.9	1.9	2.1

of conserved quantities and fluxes can significantly impact the performance of schemes even for problems at a low Mach number. We have also performed a smooth density advection test described by LW03 and found similar convergence results.

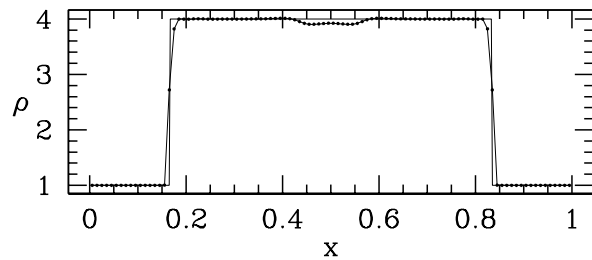


Figure 6. One-dimensional Noh problem. The analytic solution is shown with a solid line, and the numerical solution is shown with connected dots. WHAM does not exhibit any Gibbs phenomenon near the two strong shocks and has a very small dip in density at the centre.

5.5 Noh

This is a one-dimensional Riemann problem that tests the ability of codes to handle infinite-strength shocks and tests the faithfulness of reproduction of shock-shock interaction. Initially, two streams are plunging into each other symmetrically with a constant velocity. As a result of their interaction, two shocks develop that travel away from each other and leave matter behind at rest with a constant density and pressure (see figure 6). This test problem shows the importance of reducing to lower order in strong shocks. If we run this problem without any stencil reduction or eigenvector decomposition (see section 3.4), the result exhibits significant Gibbs phenomenon. Even the second order HARM scheme, which uses the MC limiter for spatial reconstruction, produces post-shock oscillations in density with an amplitude of about 5%. With WHAM, such post-shock oscillations are absent and the dip in density at the centre is also small. Our scheme's result is comparable to that of the WENO-5 scheme and is superior to that of PPM from the study of LW03. The WENO-5 scheme uses field-by-field decomposition that helps it avoid oscillations (see section 3.4); the PPM scheme uses a form of stencil reduction (so-called flattening, see Colella & Woodward 1984) that locally lowers the order of the scheme to first order near shocks. For the latter scheme the dip at the centre is large and some post-shock oscillations are visible.

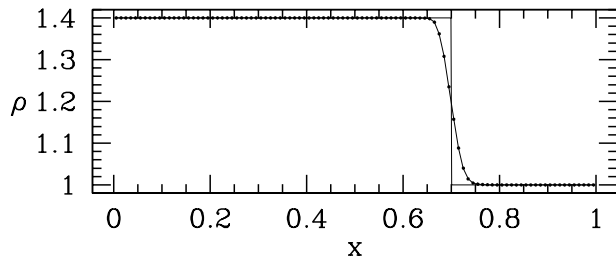


Figure 7. Moving contact problem. The analytic solution is shown with a solid line, and the numerical solution is shown with connected dots. WHAM exhibits only a moderate diffusion of the contact discontinuity despite avoiding eigenvector decomposition.

5.6 Moving contact

Figure 7 shows a test that measures the amount of diffusion of contact discontinuities in the numerical scheme. In the exact solution the initially sharp contact discontinuity remains sharp throughout the evolution. Used alone, the component-wise WENO-type reconstruction would lead to excessive smearing of the contact discontinuity because it does not use the full stencil inside the steeply changing density profile: it chooses the one-sided stencil inside of the discontinuity. To avoid this excessive smearing, we force the use of the full stencil in the regions where the polynomial fit due to the full stencil and all of its derivatives are monotonic (see Appendix A5). Our result is comparable to that of WENO-5 scheme, which uses eigenvector decomposition, from LW03.

5.7 Test 4 problem from LW03

In this problem the high resolution (small width) of the contact discontinuity, located in figure 8 at $x \approx 0.7$, and the absence of oscillations in the two high density regions are important. The numerical solution is complicated by the fact that both of these regions are ‘built-up’ as a result of the decay of an initial discontinuity. The HARM scheme exhibits post-shock oscillations at the level of about 5% in the left built-up state. WHAM does not exhibit such Gibbs phenomenon. The resolution of the contact discontinuity in our scheme is as good as that of the WENO-5 scheme from LW03, which requires eigenvector decomposition. The resolution of the contact by WHAM is the same or better than that of other schemes studied by LW03; except the PPM scheme, which uses an artificial contact discontinuity sharpening technique (Fryxell et al. 2000), a Lagrangian-remap version of PPM called VH1 (Blondin et al. 1991), and the WAFT scheme that uses the HLLC Riemann solver.

5.8 Shock – entropy wave interaction test problem

This test (figure 9) challenges the ability of the code to handle the interaction of a shock and a smoothly varying flow. Most second order schemes (Liska & Wendroff 2003b) including HARM provide inadequate resolution of the wave structure resulting from the interaction of the shock with the stationary density wave. WHAM is able to accurately resolve the high-frequency waves that develop behind the shock and provides, without the use of eigenvector decomposition, a

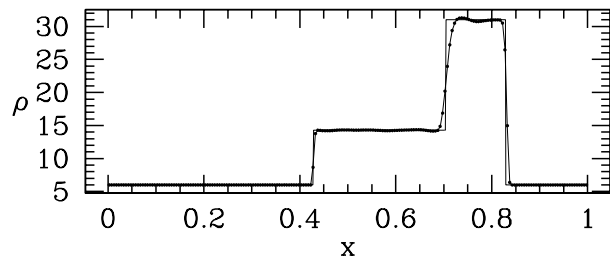


Figure 8. Test 4 from LW03. The analytic solution is shown with a solid line, and the numerical solution is shown with connected dots. The figure shows that WHAM accurately resolves the structure of this complicated Riemann problem. In particular, it provides good resolution of the moving contact discontinuity.

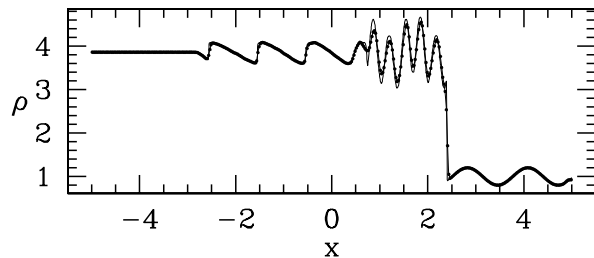


Figure 9. Snapshot of the density distribution for the shock – entropy wave interaction problem at the final time. The converged solution (at the resolution of 2000 grid cells) is shown with the solid line, and the numerical solution is shown with connected dots. WHAM accurately resolves the interaction of the shock and the smooth flow.

comparable result to that of the CWENO-5 (Qiu & Shu 2002) and WENO-5 (Liska & Wendroff 2003b) schemes that use this decomposition.

5.9 Nonrelativistic 2D Riemann problem

We have run all two-dimensional test problems from LW03 and the results of our code are comparable to those of other codes presented there. We picked the particular test problem 4 to show here because it is the only one that exhibited any noticeable Gibbs phenomenon. The initial conditions for this test problem are shown in table 4. The problem is computed at a resolution of 400×400 and uses $\Gamma = 1.4$. This test problem initially contains 4 planar shocks. Figure 10 shows the final state of the problem where a high-density eye-shaped area develops, bounded by two shocks. Even though stationary contacts are slightly less resolved in our code than in other schemes, for moving types of contact we are the same or more accurate.

5.10 2d Noh

This is a 2-dimensional version of the Noh problem for an ideal gas with $\Gamma = 5/3$ set up in Cartesian coordinates. Initially, the flow is cylindrically symmetric and converging on to the origin with a constant radial velocity, $v_r = 1$. The density distribution is uniform, $\rho = 1$, and the pressure is zero. Since the flow converges to a point, an outgoing shock develops as can be seen in figure 11. The shock position is

Table 4. Initial conditions of the nonrelativistic two-dimensional Riemann problem, test case 4 from LW03. The final time for this test problem is $t_F = 0.25$, and $\Gamma = 1.4$. The upper row of the table lists the initial state of the upper left and right corners of the Riemann problem: the ‘L’ and the ‘R’ indices stand for the left and right states, respectively. The lower row lists the lower two states. Otherwise the notation is the same as in table 1.

ρ_L	$v_{x,L}$	$v_{y,L}$	p_L	ρ_R	$v_{x,R}$	$v_{y,R}$	p_R
0.5065	0.8939	0.0	0.35	1.1	0.0	0.0	1.1
1.1	0.8939	0.8939	1.1	0.5065	0.0	0.8939	0.35

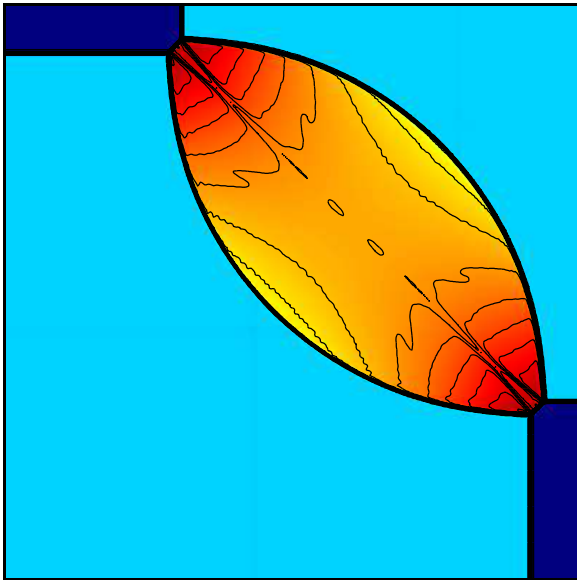


Figure 10. 2D nonrelativistic Riemann problem, case 4 from LW03, see section 5.9. Pressure is shown in color (red denotes high values and blue low values) overlaid by a set of density contours going from 0.52 to 1.92 with a step of 0.05, the same as in LW03 for easier comparison. WHAM accurately resolves the density structure in the eye-shaped area. The minor oscillations are comparable to other published results.

located at $R = R_s = t/3$, where $R = \sqrt{x^2 + y^2}$. In the post-shock region ($R < R_s$) the density is $\rho = 16$, the velocity is zero and the pressure is $p_g = 16/3$. In the pre-shock region ($R > R_s$) the density is $\rho = 1 + t/R$, the velocity stays constant $|\mathbf{v}| = 1$, and the pressure remains zero (Noh 1987; Liska & Wendroff 2003a). The initial conditions are evolved until $t_F = 2$. We use a resolution of 400×400 cells. Further, for consistency with LW03, we initialize the pressure with a small value $p_g = p_0 = 10^{-6}$ so that it is dynamically unimportant.

This test problem is unusual in that most of the final state is determined by the time-dependent boundary conditions. In contrast to the one-dimensional Noh problem, here the boundary conditions have to be the *evolved* initial conditions. For each of the Runge-Kutta substeps we set the time we use for the boundary conditions to correspond to the time of that trial time step. We find that using $p_g = p_0$ for the boundary condition as is done in, e.g., LW03, results

in a sharp kink in pressure along the diagonal in the region of influence of the boundary conditions. To avoid this, instead of keeping the pressure constant at the boundary, we use an approximate solution for the pressure $p_g = p_0(1 + \Gamma t/R)$ in the pre-shock region. We obtain this approximate solution by solving the internal energy advection equation,

$$\frac{\partial u_g}{\partial t} + \frac{1}{R} \frac{\partial}{\partial R} [R(u_g + p_g)v] = 0, \quad (32)$$

with an initial condition $p_g = p_0$ and with all other quantities determined by the above analytic solution (i.e. we neglect the effect of the pressure force on the evolution of density and velocity). We have not found a closed analytic solution to this problem for a nonzero initial pressure.

The smooth pre-shocked region is a highly supersonic flow with an initial Mach number of $M \approx 775$. For the evolution of the internal energy to be accurate in this supersonic region, the truncation error has to be small. We find that for this both the de-averaging of the conserved quantities and the transversal averaging of the fluxes are important. If we do not perform either of these two operations, the internal energy in the smooth region becomes negative. We expect that any scheme, such as PPM used in LW03, that ignores the difference between points and averages will generate a significant error in the internal energy in the pre-shock region.

The numerical results are shown in figure 11 and are much superior to those of HARM and the other schemes considered by LW03. The numerical solution is very smooth in the pre-shock region and does not show any visible oscillations for radii far enough ($r \gtrsim 0.2$) from the origin in the post-shock region except near the shock. The solution for density remains accurate even if we use $p_g = p_0$ for the boundary condition. This should be contrasted to the results of other codes, all of which show much more significant oscillations both in the pre-shock and post-shock regions.

5.11 Implosion

The implosion test problem (LW03) corresponds to the interaction of a low-density, low-pressure diamond ($\rho_i = 0.125$, $p_i = 0.14$) with a high-density, high-pressure exterior ($\rho_o = 1$, $p_o = 1$) in a square box with reflecting boundaries, both the diamond and the box centred on the origin. The gas adiabatic index is $\Gamma = 1.4$. The vertices of the diamond are located at the intersections of coordinate axes with a circle of radius 0.15. The computational box is $(-0.3, 0.3) \times (-0.3, 0.3)$. Initially the velocities are zero. We perform the computations only for the upper-right quadrant of the box (as in LW03 we use reflecting boundary conditions on all 4 boundaries) at a resolution of 400×400 . In order to avoid grid-induced artifacts in the initial conditions, for grid cells intersected by the discontinuity we use the average of the two states. The initial discontinuity evolves into two shocks with a contact discontinuity between them.

The interaction of the contact discontinuity with the shocks generates streams that travel toward the origin and, after colliding there, form an outflow in the form of a narrow jet. Figure 12 shows the configuration at the final time $t_F = 2.5$. This problem tests the ability of the code to resolve contact discontinuities and maintain symmetry in two dimensions: if a code does not preserve symmetry, the jet will

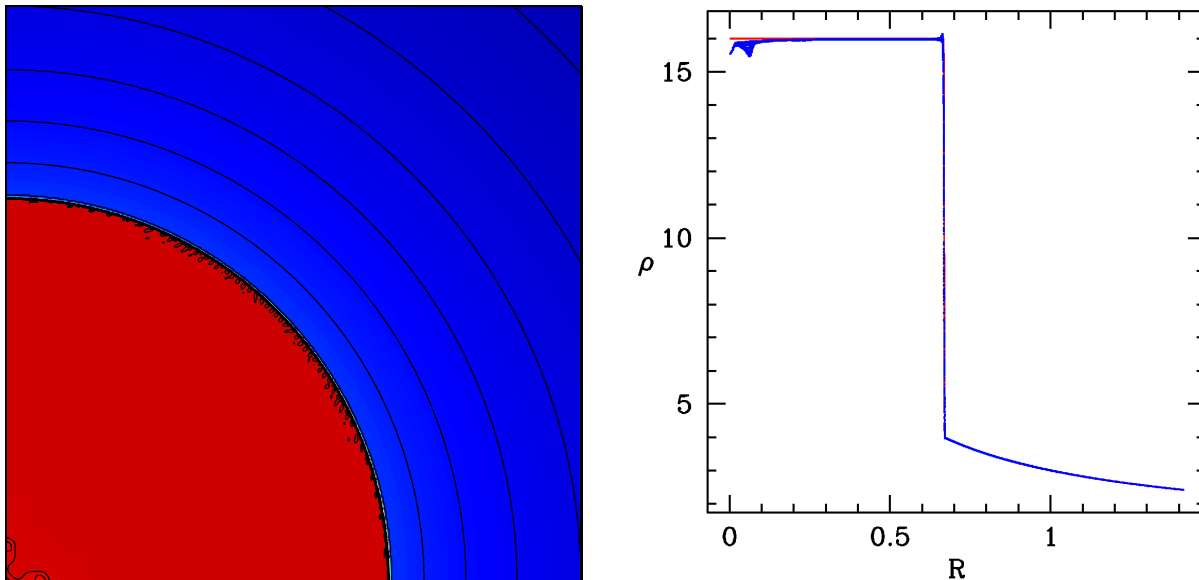


Figure 11. Density distribution in the two-dimensional Noh problem at the final time $t_F = 2$. The left panel shows density both in color (red denotes high values and blue low values) and by a set of contours going from 2.5 to 4 in steps of 0.25 and from 14 to 17 in steps of 0.2, the same as in LW03. The right panel shows the scatter plot of density w.r.t. radius (blue dots) and the analytic solution (thin red line). WHAM provides a very accurate solution in the pre-shock region and shows significantly fewer oscillations behind the shock compared to other schemes. For the left panel, the noise near the shock appears because one of the contours is chosen to the analytic value.

not be produced or will be distorted. Lower order schemes significantly diffuse the jet at this resolution. Unlike some of the schemes from LW03, our code gives exactly symmetric results. Further, the resolution of the jet provided by our code is comparable to that of the WENO-5 scheme from LW03 and is superior to all other schemes discussed in that paper and HARM. Since Athena has a lower dissipation than WHAM, their jet head travels about 10% further (Stone 2006). The result obtained with WHAM could be improved if we use an approximate HLLC Riemann solver, which provides a better resolution for contact discontinuities.

5.12 Explosion

The explosion problem verifies the ability of the code to evolve unstable contacts. In particular this problem studies how sensitive the code is to numerical perturbations, which arise from the discreteness of the grid.

The initial conditions are cylindrically symmetric, with a high-density, high-pressure cylinder, $\rho_i = 1$, $p_i = 1$, with a radius of 0.4, embedded in a low-density, low-pressure medium, $\rho_o = 0.125$, $p_o = 0.1$. The gas constant is $\Gamma = 1.4$. As in LW03, we perform the computations in Cartesian coordinates in a square box $(0, 1.5) \times (0, 1.5)$ at a resolution of 400×400 grid cells, with reflecting boundary conditions at the left and bottom boundaries and zero-derivative conditions at the upper and right boundaries. The initial discontinuity evolves into two shocks with a contact discontinuity in between. Figure 13 shows a snapshot of the problem at a final time of $t_F = 3.2$ after the outgoing shock leaves the computational domain through the upper and right boundaries and the ingoing shock bounces off the origin and passes through the contact discontinuity.

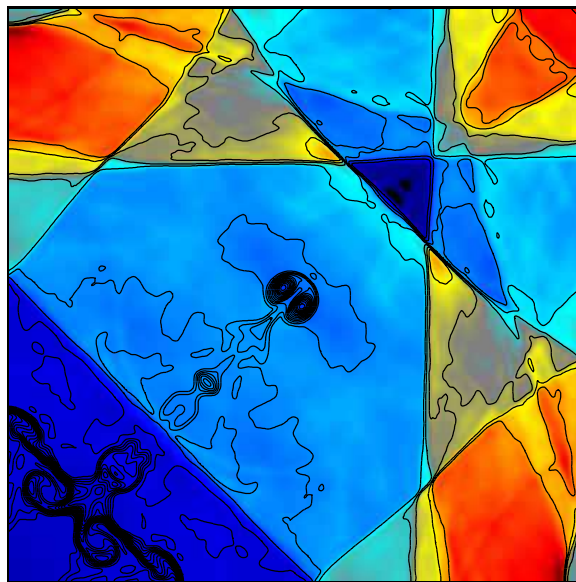


Figure 12. Implosion problem (LW03). Pressure is shown in color (red denotes high values and blue low values) overplotted by a set of density contours going from 0.35 to 1.1 in steps of 0.025, the same as in LW03. The figure shows that WHAM is able to maintain perfect symmetry of the solution and has low diffusivity that is required for producing the narrow jet.

The interface of the contact discontinuity in this test is unstable to perturbations, so the initial conditions have to be properly averaged for grid cells that are intersected by the discontinuity to avoid seed perturbations in the contact discontinuity coming from the grid structure in the initial

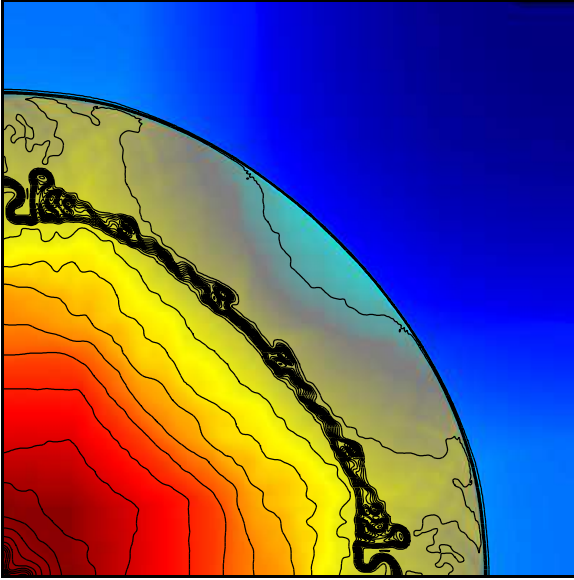


Figure 13. Explosion problem (see, e.g., LW03). Pressure is shown in color (red denotes high values and blue low values) overplotted by a set of density contours going from 0.08 to 0.21 in steps of 0.005, the same as in LW03. WHAM shows the same or smaller degree of breakup of the unstable contact discontinuity compared to the WENO-5 scheme from LW03.

conditions. However, one cannot fully avoid perturbations to the contact discontinuity, and the discontinuity breaks up similarly to the way it happens for other high order schemes (LW03). As pointed by LW03, this problem is sensitive to the conditions that are applied at the upper and right boundaries. Therefore, the interaction of these boundary conditions with the flow and, in particular, the contact discontinuity could seed additional perturbations to the contact discontinuity. The width and degree of break up of the contact discontinuity is the same as or smaller than that of the WENO-5 scheme in LW03. However, unlike the WENO-5 scheme, our result is obtained without the use of eigenvector decomposition.

5.13 Moving Gresho problem

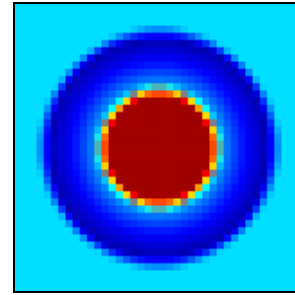
This problem tests how well a numerical scheme is able to advect a smooth vortex supported by the balance of pressure and rotation. A non-moving vortex centred at $(0, 0)$ has the following distribution of velocity and pressure in polar coordinates (r, φ) with the origin at its centre:

$$\begin{aligned} v_\varphi &= 5r, & p_g &= 5 + \frac{25}{2}r^2, & 0.0 \leq r < 0.2, \\ v_\varphi &= 2 - 5r, & p_g &= 9 + \frac{25}{2}r^2 - 20r + 4 \ln 5r, & 0.2 \leq r < 0.4, \\ v_\varphi &= 0, & p_g &= 3 + 4 \ln 2, & 0.4 \leq r, \end{aligned}$$

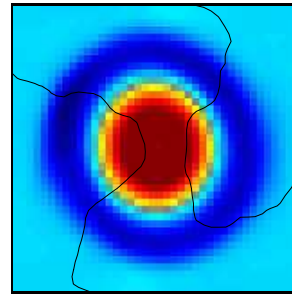
the radial velocity v_r is zero, the density is unity, and the polytropic index of the gas is $\Gamma = 1.4$. In the test, this vortex is initially imparted unit velocity in the x -direction. Figure 14 shows snapshots of the vortex at the initial time and the final time $t_F = 3$ when the vortex centre has moved to $(3, 0)$. We perform the computation in cartesian coordinates in the rectangle $(-0.5, 3.5) \times (-0.5, 0.5)$ at a resolution of

Table 5. Relative L_1 -errors for the Moving Gresho problem (sec. 5.13). The errors are computed over the core of the vortex within radius 0.2 from the vortex centre, at the final time $t_F = 3$. WHAM makes about a factor of 5 smaller error in baryon density and internal energy than HARM at the resolution of 160×40 .

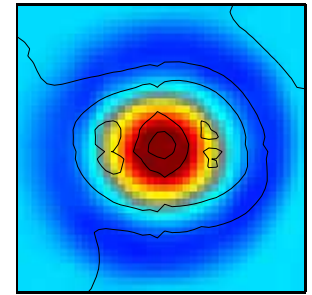
Scheme	$\Delta_R \rho$	$\Delta_R u_g$	$\Delta_R v_x$	$\Delta_R v_y$
WHAM	1.68e-03	3.90e-03	2.10e-02	1.09e-02
HARM	8.36e-03	2.61e-02	3.87e-02	2.06e-02



(a) Initial



(b) Final WHAM



(c) Final HARM

Figure 14. Moving Gresho problem (see, e.g., LW03). Initial (a) and final (b) & (c) distributions of vorticity are shown in color (red denotes high values and blue low values) overplotted by a set of density contours going from 0.97 to 1.03 in steps of 0.006, the same as in LW03. The resolution of the fragments shown is 40×40 , the resolution of the full grid is 160×40 . The WHAM scheme (panel b) preserves the structure of the vortex in density and velocity exceptionally well compared to HARM (panel c) and the various schemes considered in LW03.

160×40 and use zero-derivative outflow boundary conditions at all boundaries. This is the same as used by LW03.

WHAM does extremely well in preserving the structure of the vortex in both velocity and density. Our code maintains the vorticity and makes a very small error in density so that it ends up with much fewer density contours compared to HARM and all schemes in LW03. HARM as well as the codes considered in LW03 such as WENO-5, PPM, VH1, etc., destroy the shape of the vortex, making it ellipsoidal and/or significantly diffuse in the radial profile. This shows the superiority of our high accuracy finite-volume approach in applications involving smooth problems. Relative L_1 -errors of the final solution at $t_F = 3$ w.r.t. to the analytic solution for WHAM and HARM are shown in table 5.

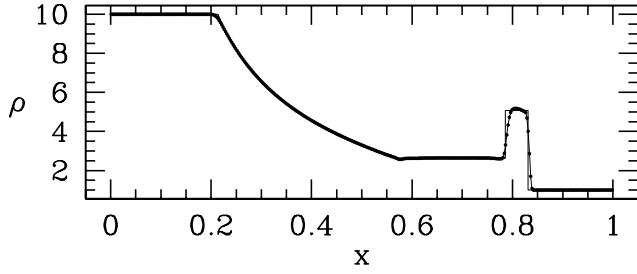


Figure 15. The distribution of density at the final time of the one-dimensional relativistic Riemann problem 1 from ZM06. The numerical solution is shown with connected dots, and the analytical solution is shown with the solid line. WHAM correctly reproduces all ingredients of flow: the rarefaction wave, the contact discontinuity, and the shock.

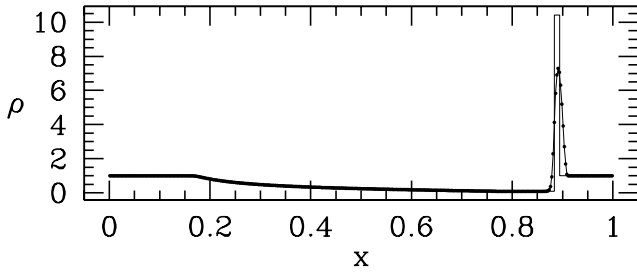


Figure 16. Density distribution for the one-dimensional relativistic Riemann problem 2 from ZM06. The numerical solution is shown with connected dots, and the analytical solution is shown with the solid line. WHAM performs well by getting the height of the built-up state to about 70% of the analytic value, a height comparable to other codes (Zhang & MacFadyen 2006; Morsony et al. 2006).

5.14 1D relativistic Riemann problem 1

The initial conditions are given in table 1. This problem verifies the ability of a numerical scheme to treat basic relativistic problems. As seen in figure 15, the initial discontinuity decays into a rarefaction wave, a contact discontinuity, and a shock. The resolution of the contact discontinuity and the amount of post-shock oscillation is comparable to that of the WENO scheme in ZM06. Note that our code achieves a comparable result despite not using the characteristic decomposition that certainly helps the resolution of Riemann problems. Table 6 shows the L_1 -errors of the solution and the order of convergence of WHAM for this problem as well as the following five relativistic Riemann problems.

5.15 1D relativistic Riemann problem 2

The data for this test are given in table 1. This is a challenging test with sparse resolution. It is very hard to get the correct height of the built-up state due to the smearing of the contact discontinuity and the proximity of the shock (figure 16). Comparable to that of other codes (Aloy et al. 1999; Zhang & MacFadyen 2006; Morsony et al. 2006), WHAM gets the height of the built-up state to about 70% of the analytic value.

Table 6. Absolute and relative L_1 errors in density and the order of convergence of WHAM for relativistic Riemann problems 1 – 6. For a unit interval, at which these problems are set up, the definition of the absolute L_1 error (28) is equivalent to the definition used by ZM06. WHAM converges at approximately first order for all tests, where the errors and convergence rates are similar to other published work.

Problem	Resolution	$\Delta_A \rho$	$\Delta_R \rho$	Order	Section
1	100	1.39e-01	1.39e-02	–	5.14
	200	7.26e-02	7.26e-03	0.94	
	400	3.57e-02	3.57e-03	1.00	
	800	2.08e-02	2.08e-03	0.78	
	1600	1.06e-02	1.06e-03	0.97	
3200	5.59e-03	5.59e-04	0.93		
2	100	2.12e-01	2.04e-02	–	5.15
	200	1.48e-01	1.42e-02	0.52	
	400	9.40e-02	9.03e-03	0.65	
	800	5.17e-02	4.96e-03	0.86	
	1600	2.57e-02	2.47e-03	1.00	
3200	1.52e-02	1.46e-03	0.76		
3	100	9.32e-02	1.41e-02	–	5.16
	200	5.91e-02	8.97e-03	0.66	
	400	3.46e-02	5.24e-03	0.78	
	800	1.93e-02	2.93e-03	0.84	
	1600	1.04e-02	1.58e-03	0.89	
3200	5.56e-03	8.43e-04	0.91		
4	100	6.20e-01	2.63e-02	–	5.17
	200	3.60e-01	1.53e-02	0.79	
	400	2.01e-01	8.55e-03	0.84	
	800	1.02e-01	4.34e-03	0.98	
	1600	6.79e-02	2.88e-03	0.59	
3200	3.57e-02	1.51e-03	0.93		
5	100	6.88e-01	1.54e-01	–	5.18
	200	5.96e-01	1.34e-01	0.21	
	400	4.13e-01	9.24e-02	0.53	
	800	2.68e-01	6.00e-02	0.62	
	1600	1.47e-01	3.30e-02	0.86	
3200	7.83e-02	1.75e-02	0.91		
6	25	7.18e03	2.54e-02	–	5.19
	50	4.57e03	1.62e-02	0.65	
	100	1.73e03	6.11e-03	1.4	
	200	1.14e03	4.04e-03	0.6	
	400	4.24e02	1.50e-03	1.4	
	800	2.82e02	9.96e-04	0.59	
	1600	1.04e02	3.67e-04	1.4	
3200	6.91e01	2.44e-04	0.59		

5.16 1D relativistic Riemann problem 3

The initial discontinuity in this problem generates two shocks and a contact discontinuity, see figure 17. Table 1 lists the problem parameters. The slow moving reverse shock appears to be hard for most codes to handle. Even the most dissipative second order schemes like MINMOD produce oscillations at a noticeable level. Our code exhibits them too at about twice the level of second order codes that do not use eigenvector decomposition. We note that the relativistic version of the FLASH code, which uses a flattening pro-

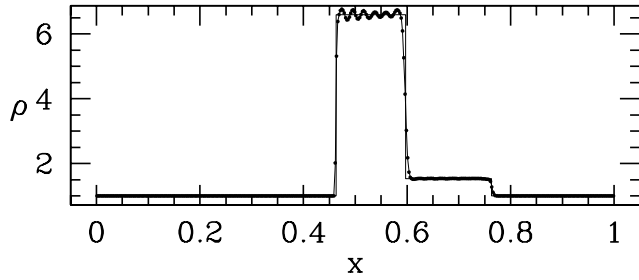


Figure 17. Density distribution of the one-dimensional relativistic Riemann problem 3 from ZM06. The numerical solution is shown with connected dots, and the analytical solution is shown with the solid line. This figure shows that WHAM gets the positions of discontinuities correctly but sometimes produces small amplitude oscillations near slowly moving shocks. Similar oscillations are present at some level in most codes that do not use eigenvector decomposition (ZM06).

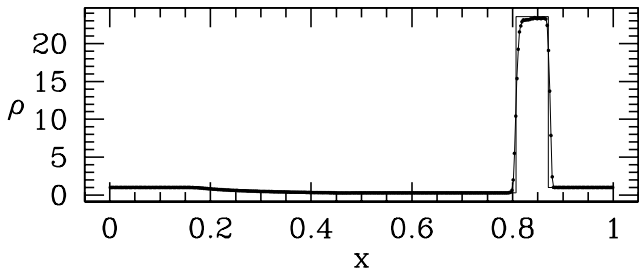


Figure 18. One-dimensional relativistic Riemann problem 4 from ZM06. WHAM is able to accurately resolve the contact discontinuity and the height of the built-up state for this flow that has a large shearing velocity.

cedure to decrease the order of the scheme to first order in shocks, does not produce post-shock oscillations for this test (Morsony et al. 2006). However, this flattening procedure requires parameter tuning for strong shocks (see section 5.19).

5.17 1D relativistic Riemann problem 4

The two initial states in this test have a large shearing velocity (table 1). Shearing flows are intrinsically hard in the relativistic case because of the coupling between the directions through the Lorentz factor. This configuration, however, does not lead to problems. Figure 18 shows that the width of the contact discontinuity is the same as that of the WENO code from ZM06; in our case, without the use of eigenvector decomposition, the built-up state near the contact discontinuity slightly undershoots compared to the analytic value.

5.18 1D relativistic Riemann problem 5

This test is very similar to the previous one in terms of the initial conditions (table 1). In this case, however, there is no shear; rather, both states are moving at a relativistic velocity in the transverse direction. Figure 19 shows that at a moderate resolution of 400 cells WHAM gets the positions of the

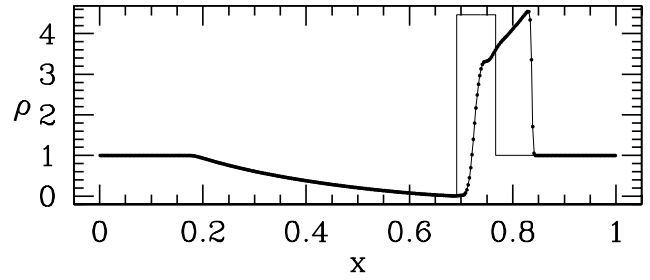


Figure 19. Density distribution for the one-dimensional relativistic Riemann problem 5 from ZM06. For large transverse velocities as in this problem, one has to use an increased resolution in order to obtain the correct positions of discontinuities.

discontinuities incorrectly. In order to get reasonable convergence to the analytic solution, one has to use an increased resolution for this test. Our code's result agrees with that of other codes at the same resolution (Zhang & MacFadyen 2006; Morsony et al. 2006).

5.19 1D relativistic Riemann problem 6

This is a very stringent test that probes the ability of a code to handle flows at extremely large Lorentz factors with strong shocks. It is a generalization of the nonrelativistic one-dimensional Noh problem (section 5.5) in which a highly relativistic flow with $\gamma \approx 7 \times 10^4$ hits a reflecting boundary (see table 1). Figure 20 shows that a reverse shock forms at the boundary $x = 1$ and moves to the left leaving the matter behind at rest.

WHAM produces minimal post-shock oscillations comparable to other schemes, such as a WENO code that uses eigenvector decomposition (ZM06). In the post-shock region the density reaches a maximum relative error of 1.5% in the vicinity of the reflecting wall. This is twice as small as with WENO (ZM06) and HARM. Unlike the PPM algorithm (ZM06), we do not have to perform any fine-tuning of our code parameters for this test.

A similar yet more extreme test is discussed by Aloy et al. (1999) for which they chose $\gamma = 2.24 \times 10^5$, $p = 7.63 \times 10^{-6}$, and a resolution of 200 grid cells. As shown in Appendix A10, their test problem can be barely resolved by a computer with a machine accuracy of $\sim 10^{-16}$ (i.e. double precision). In order to minimize post-shock oscillations, they chose a Courant factor of 0.1 and tuned their reconstruction parameters. Using WHAM's standard numerical settings (e.g. Courant factor of 0.5), we obtain an error of $\lesssim 0.5\%$ in all quantities for this test, an error similar to that of Aloy et al. (1999) (here we use their definition of relative error). The errors are dominated by the numerical solution having a shock width of a few points.

5.20 2D relativistic shock-tube problem

The initial conditions for this problem are shown in table 7. The test is run at a resolution of 400×400 until $t_F = 0.4$. The contour plot of density is shown in figure 21. This is a difficult highly relativistic two-dimensional Riemann problem (Del Zanna & Bucciantini 2002; Lucas-Serrano et al. 2004; Zhang & MacFadyen 2006; Morsony et al. 2006). The

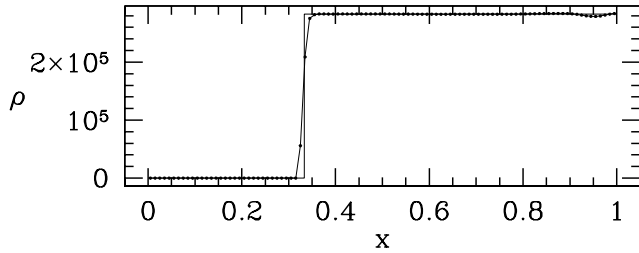


Figure 20. Density distribution for the one-dimensional relativistic Riemann problem 6 from ZM06. The numerical solution is shown with connected dots, and the analytical solution (ZM06) is shown with a solid line. WHAM is able to evolve extremely relativistic supersonic flows with strong shocks with minimal Gibbs phenomenon.

Table 7. Initial conditions for the two-dimensional relativistic shock-tube problem (Del Zanna & Bucciantini 2002), see section 5.20. The notation is the same as in table 4. The problem is computed on the domain $(0, 1) \times (0, 1)$ at a resolution of 400×400 until time $t_F = 0.4$ with $\Gamma = 5/3$.

ρ_L	$v_{x,L}$	$v_{y,L}$	p_L	ρ_R	$v_{x,R}$	$v_{y,R}$	p_R
0.1	0.99	0.0	1.0	0.1	0.0	0.0	0.01
0.5	0.0	0.0	1.0	0.1	0.0	0.99	1.0

Lorentz factor reaches values larger than 25 inside the sharp diagonal jet-like feature in the lower left quadrant. The amount of oscillation in the lower-left quadrant is less than with the relativistic FLASH code (Morsony et al. 2006) and the RAM code (ZM06), which uses finite-difference fifth order WENO with field-by-field decomposition. WHAM does not use such decomposition. The resolution of the diagonal feature in the upper-right quadrant is comparable to RAM.

5.21 2D relativistic jet in cylindrical geometry

We study a two-dimensional relativistic jet in cylindrical geometry. This problem couples many elements, which were separately tested in the individual problems described so far, in a real astrophysical setting: relativistic, highly supersonic flow, containing strong relativistic shocks, shear flows, and instabilities. Along with being of astrophysical significance, this test allows us to benchmark our numerical scheme against others. For the sake of comparison, we have used the same conditions for the test as Zhang & MacFadyen (2006) and Marti et al. (1997, model C2). The size of the computational domain is $(0, 15) \times (0, 45)$ in the (R, z) plane, and we use a resolution of 384×1152 . The ambient medium is initially at zero velocity, with density $\rho_m = 1$ and pressure $p_m = 0.000170305$. The jet is injected along the z -axis from the lower boundary with a density of $\rho_b = 0.01$, pressure equal to the ambient pressure, $p_b = p_m$, and a speed of $v_b = 0.99c$, which corresponds to a Lorentz factor of $\gamma \approx 7$. Numerically, we implement the injection by assigning the values of the boundary grid cells within $R < 1$, $z < 0$ to the state of the jet material. We use the zero-derivative outflow boundary conditions at the low- z ($R \geq 1$), high- z , and high-

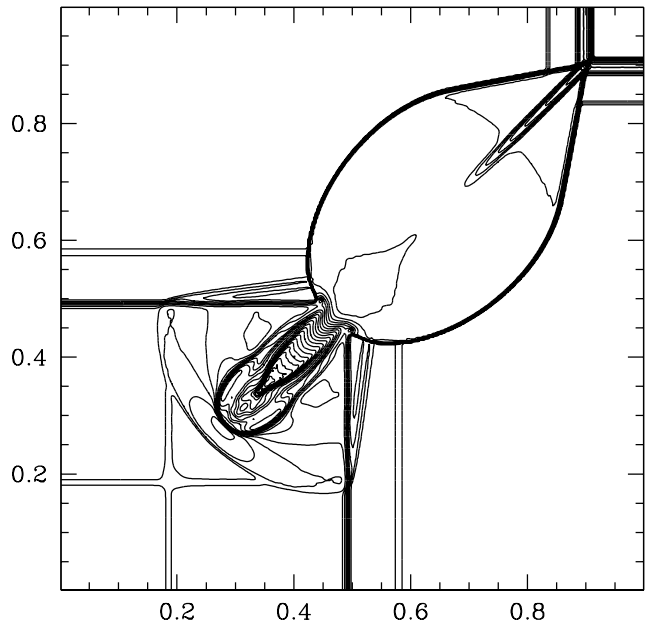


Figure 21. 2D relativistic Riemann problem (Del Zanna & Bucciantini 2002; Zhang & MacFadyen 2006) at the final time $t_F = 0.4$, see section 5.20. The plot shows 30 equally spaced contours of $\log_{10} \rho$ that go from -2.241 to 0.8243 in steps of 0.1057 . WHAM is able to handle highly relativistic multidimensional flows with minimal Gibbs phenomenon.

R boundaries and use the appropriate boundary condition on the axis $R = 0$. We evolve the system until $t_F = 100$.

The interaction of the jet material with the ambient medium forms an expanding bow shock and a Mach shock with a contact discontinuity in between that goes Kelvin-Helmholtz unstable, see figure 22. The jet contains internal shocks, backflows, and shear flows. The jumps in the γ -factor on the right panel of the figure correspond to relativistic shocks crossing the axis of the jet. The essential structure of the jet, its head position, the shape of the bow shock, and the development of the Kelvin-Helmholtz instability agree with other codes' results (Marti et al. 1997; Zhang & MacFadyen 2006).

5.22 Bondi flow in Schwarzschild geometry

We study the order of convergence of our the scheme for stationary spherically symmetric accretion on to a non-spinning black hole (Bondi 1952). Even though the exact solution is spherically symmetric, for WHAM in 2D the Bondi problem is in fact two-dimensional: in the θ -momentum equation, a gradient of momentum flux ($\partial_\theta(p_g \sin \theta)$ in the non-relativistic limit) is balanced by a source term ($p_g \cos \theta$) that numerically cancel out to within the truncation error (Gammie et al. 2003). We find that in order to obtain an accurate solution, one has to properly average the source terms on the r.h.s. of the equations of motion (6). Further, for this test WHAM uses Kerr-Schild coordinates that have nonzero space-time mixing even for the case of a non-spinning black hole: 7 out of 10 components of the metric are nonzero, so this problem involves many of the terms that appear in the general equations of motion. For this test

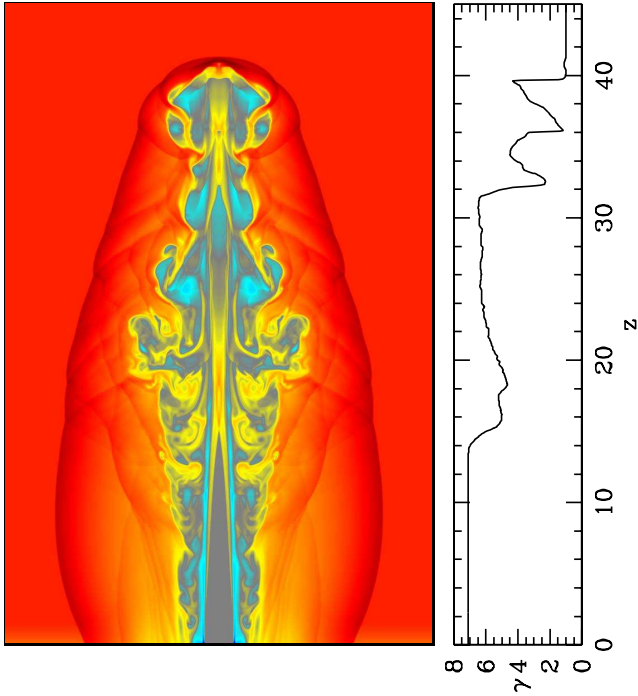


Figure 22. Relativistic two-dimensional jet problem in cylindrical geometry: the left panel shows the color-coded distribution of the logarithm of the fluid frame rest-mass density (red denotes high values and blue low values), and the right panel shows the z -dependence of γ along the axis of the jet. The simulation was run at a resolution of 384×1152 , the same as in ZM06, and the result is mirrored across the axis in order to obtain the figure in the left panel. For more detail, see section 5.21. WHAM reproduces all essential elements of the jet structure for this astrophysically relevant problem.

problem we set the source term analytically in order to test convergence near machine precision accuracy.

We follow the setup of the problem as discussed by Hawley et al. (1984); Gammie et al. (2003). We fix the radius of the sonic surface, $R_s = 8$, the adiabatic index of the gas, $\Gamma = 4/3$, the gas adiabat, $K = 1 (= p_g/\rho^\Gamma)$, and choose the mass of the black hole, $M = 1$. These determine the critical solution and the three integrals of the problem: the radial flux of mass ($= \sqrt{-g}\rho u^r$), the flux of energy ($= T^r_t$), and the entropy of the flow. The solution can be found semi-analytically by solving an 8th order polynomial equation for the temperature of the flow (Hawley et al. 1984).

We treat the boundary conditions as follows. We use the value of the ‘baryon flux’ C_1 from the outermost active grid cell together with the critical values of K and the ‘energy flux’ C_2 to set the state of the outer- r boundary cells (for definitions of the integrals C_1 and C_2 , see Hawley et al. 1984). At the inner- r boundary we choose the states of the cells to correspond to the three integrals of the flow determined from the numerical solution at the innermost active grid cell in the active grid. At the θ -boundaries we use the usual polar axis boundary conditions. As the system approaches steady state, the mass flux is determined by the critical condition at the sonic surface. Since in steady state the fluxes become uniform in space within the truncation error, extrapolating the flux allows us to approximate the

Table 8. Relative L_1 -errors in density and the order of convergence of the WHAM, HARM, and WHAM-IS schemes for the 1D and 2D spherical accretion problems (section 5.22), at $N \times N$ resolution. At the same resolution, the higher order WHAM scheme provides a much smaller error than the other two schemes. The averaging of the source terms is crucial for preserving the high order accuracy. Radial velocity and internal energy similarly converge to the analytic solution.

N	16	32	64	128	256	512
1D Bondi problem						
WHAM	1.6e-5	1.8e-7	1.5e-9	1.6e-11	1.2e-12	5.0e-15
Order	—	6.4	6.9	6.6	3.7	7.9
HARM	9.7e-4	2.1e-4	4.9e-5	1.2e-5	2.8e-6	6.9e-7
Order	—	2.2	2.1	2.0	2.0	2.0
WHAM-IS	2.0e-3	5.2e-4	1.3e-4	3.2e-5	7.9e-6	2.0e-6
Order	—	2.0	2.0	2.0	2.0	2.0
2D Bondi problem						
WHAM	1.6e-5	1.8e-7	1.5e-9	1.6e-11	1.2e-12	4.9e-15
Order	—	6.4	7.0	6.5	3.7	7.9
HARM	6.4e-4	1.6e-4	3.9e-5	9.7e-6	2.4e-6	6.0e-7
Order	—	2.0	2.0	2.0	2.0	2.0
WHAM-IS	1.4e-3	3.3e-4	8.2e-5	2.0e-5	5.1e-6	1.3e-6
Order	—	2.0	2.0	2.0	2.0	2.0

boundary conditions very accurately, compared to extrapolating, e.g., the nontrivially varying density. This also avoids the order of the extrapolation limiting the order of convergence of the scheme.

We have performed the problem in 1D and 2D in modified Kerr-Schild coordinates, the same coordinate system as in Gammie et al. (2003), over the domain $r \in (1.9, 20)$ in units of GM/c^2 . We initialize the problem with the analytic solution and let the system evolve for $t = 1000$ in units of GM/c^3 , corresponding to several sound crossing times, by which time the system reaches steady state. We then compute the relative L_1 -error norm in density between the final solution and the initial conditions over the active grid. The results are shown in table 8 for various resolutions. WHAM converges at an order higher than 5 and makes a much smaller error than the WHAM-IS scheme, which does not average the source terms, or the HARM scheme. The latter two schemes converge at second order as expected, since they do not properly account for the difference between the point and average source terms and/or fluxes and conserved quantities. The nonuniform convergence rate appears to be due to the sensitivity of the monotonicity indicator (see section A5) for particular parts of the solution.

5.23 Equilibrium torus in Kerr geometry

Finally, we consider a rotating fluid torus surrounding a spinning black hole that is in equilibrium under the action of pressure and centrifugal forces (Fishbone & Moncrief 1976). We choose the black hole spin to be $a/M = 0.95$, and take the following parameters for the torus: location of the inner edge $r_{\text{in}} = 3.7$, angular momentum per

Table 9. Relative L_1 -error in density and order of convergence in density of the WHAM and HARM schemes for an equilibrium torus problem, section 5.23, at $N \times N$ resolution. Similar convergence is observed in all other quantities. For this general relativistic problem in the Kerr metric, WHAM achieves asymptotic fifth order convergence.

N	16	32	64	128	256	512
WHAM	1.6e-2	1.7e-3	2.3e-4	2.8e-5	1.4e-6	2.7e-8
Order	—	3.3	2.9	3.1	4.3	5.7
HARM	1.5e-2	3.5e-3	6.6e-4	1.4e-4	3.3e-5	8.3e-6
Order	—	2.1	2.4	2.2	2.1	2.0

unit mass $u^t u_\varphi = 3.85$ (as in McKinney & Gammie 2004; Gammie et al. 2004), and equation of state $p_g = K\rho^\Gamma$ with $K = 10^{-3}$, $\Gamma = 4/3$.

The exact Fishbone & Moncrief torus solution is embedded into a vacuum. In order to avoid having zero densities that are problematic numerically, we embed the torus in a dynamically unimportant atmosphere by introducing floors on the density and internal energy: $\rho_{\min} = 10^{-4}(r/r_{\text{in}})^{-3/2}$, $u_{\min} = 10^{-6}(r/r_{\text{in}})^{-5/2}$ (as in Gammie et al. 2003).

We use the same modified Kerr-Schild coordinates as in Gammie et al. (2003), concentrating the resolution toward the midplane, and run the simulation until $t_F = 10$ in the 2D domain $(r, \theta) \in (0.98r_h, 20) \times (-\pi/2, \pi/2)$, where r_h is the radius of black hole horizon. We compute the relative L_1 -error norm between the final solution and the initial conditions over the region where $\rho > 0.02\rho_{\max}$ to minimize the influence of the atmosphere on the convergence results. The results are shown in table 9. We see that WHAM asymptotically converges at fifth order,⁸ while HARM converges at second order.

This final example tests all the general relativistic aspects of WHAM – equations of motion, metric, connection coefficients, and source terms – in Kerr space-time.

6 LIMITATIONS

The hydrodynamical numerical scheme we have described actually does include magnetic fields, with the divergence-free constraint (5d) applied using the FLUX-CT constrained transport method (Gammie et al. 2003). This method averages the fluxes of the magnetic field in such a way that the associated update to the magnetic field is guaranteed to preserve a certain numerical representation of magnetic field divergence. However, the magnetic fields are treated to lower

⁸ At low resolutions, the truncation error of WHAM is dominated by unresolved edges of the torus where the conserved quantities rapidly fall off to zero and the reconstruction becomes second order. Even though the torus is resolved with about 30 grid cells at a resolution of 64×64 , the drop of $U_0 = \sqrt{-g\rho u^t}$ at the torus edge is resolved with only 4 grid cells. Because of this, at low resolutions HARM is comparable to WHAM, but at high resolutions WHAM is far more accurate.

order than the hydrodynamical quantities. In a followup paper (McKinney, Tchekhovskoy, & Narayan in prep.), we will describe a consistent high order scheme that generalizes our hydrodynamical method to a full MHD method with a constrained transport method that is a high order version of the staggered grid method used by Athena (Gardiner & Stone 2005). We expect that the stiff regime associated with the MHD equations in the highly magnetized limit will significantly benefit from our higher-order reconstruction method since the effective magnetic Mach number is M_{mag} , which is on order of 10^3 or larger for models of black hole or neutron star systems.

WHAM is capable of performing simulations in three dimensions. However, a description of our method and a suite of 3D tests will be given in a followup paper (McKinney, Tchekhovskoy, & Narayan in prep.).

We have not implemented any performance optimizations in our scheme since much has been already optimized in HARM which WHAM is based upon. Currently, for one-dimensional problems, WHAM is about 4 times slower than the third order method used by McKinney (2006b). We expect that further optimization will lead to a factor of several speed increase and make WHAM competitive with any scheme of similar accuracy/order. Our experience suggests, however, that even without optimizations the duration of simulations will not be the bottleneck in completing science projects.

7 PROPOSED APPLICATIONS

The numerical scheme that we have developed provides superior accuracy in highly supersonic flows as well as flows in which the energy scales are very different. The applications where the scheme is particularly advantageous therefore include the study of supersonic disk winds, jets, and pulsar magnetospheres. There have been numerical studies of these systems within the force-free (Komissarov 2002, 2006; McKinney 2006a; McKinney & Narayan 2007b; McKinney 2006c; Spitkovsky 2006; Narayan et al. 2007) and full MHD (Komissarov 2005; McKinney & Gammie 2004; Bucciantini et al. 2006; McKinney & Narayan 2007a; McKinney 2006b) limits. McKinney (2006b) achieved high magnetization, $b^2/(\rho + u_g + p_g) \sim 10^3$, and could handle values of up to 10^4 but it was not clear whether the evolution was accurate in that regime. However, even such high magnetization values are still below the actual observed values of $10^5 - 10^6$ in the case of pulsar outflows.

We plan to study jet and pulsar systems in the limit of cold GRMHD, i.e. with the internal energy of the plasma vanishing exactly. This limit should allow us to achieve higher magnetisation factors more easily. Since our code does not require the use of eigenvector decomposition, only the equations of motion have to be changed to study systems in this limit.

Our code can also be used to perform three-dimensional studies of thin discs around black holes that involve highly supersonic motion in the φ -direction. Such studies would determine how jet speed and power is related to disk thickness, address the problem of the multidimensional structure of disks near the innermost stable circular orbit (Beskin & Tchekhovskoy 2005), and test the applica-

bility of well-known analytic models (Shakura & Sunyaev 1973; Novikov & Thorne 1973) there.

8 CONCLUSIONS

We have developed a high order accurate conservative finite volume general relativistic hydrodynamic (GRHD) scheme called WHAM that is robust in the vicinity of shocks and is very accurate in smooth flows even for an arbitrary metric and coordinates. It compares very well with its special relativistic hydrodynamic analogs and is, as far as we know, the first GRHD code that converges at fifth order in smooth flows. In contrast to most high order schemes (Jiang & Tadmor 1998; Titarev & Toro 2004; Feng et al. 2004; Zhang & MacFadyen 2006), WHAM uses primitive quantities to reconstruct the values of quantities at interfaces. This is a safe choice in the relativistic regime because it guarantees that the interface values, which determine inter-cell fluxes, are physical.

WHAM avoids the use of the computationally intensive eigenvector decomposition approach used by many high order schemes (Jiang & Tadmor 1998; Titarev & Toro 2004; Feng et al. 2004; Zhang & MacFadyen 2006; Xing & Shu 2006). Instead, we adaptively reduce the order of the scheme near discontinuities, while, unlike the standard WENO formalism, avoid excessive reduction in smooth monotonic flows. The resolution of contact discontinuities we obtain is comparable to that of WENO schemes that use eigenvector decomposition without contact steepeners.

Unlike finite difference schemes (e.g., Jiang & Tadmor 1998; Feng et al. 2004; Zhang & MacFadyen 2006), which conserve the integrals of motion up to truncation error, our finite volume scheme conserves them exactly, to machine precision. Our scheme performs the proper conversion between the average and point values of conserved quantities, fluxes, and source terms using fifth order WENO-type reconstruction. We find that the alternative method of quadratures is less accurate for this purpose (e.g., Titarev & Toro 2004; Noelle et al. 2006; Xing & Shu 2006).

We have demonstrated that our scheme provides accurate solutions in highly supersonic flows, which are intrinsically hard for conservative numerical schemes. In particular, the scheme is able to accurately evolve shocks for which both pre-shock and post-shock material moves supersonically through the computational grid. The scheme is likely to be particularly good for studies of relativistic and/or supersonic flows near compact objects. In the future we plan to extend the formalism to include magnetic fields and study models for which the magnetization is large to identify why present schemes have difficulties in such regimes (McKinney, Tchekhovskoy, & Narayan in prep.).

ACKNOWLEDGMENTS

We thank Charles Gammie, John Hawley, Anatoly Spitkovsky, and Jim Stone for useful discussions. We also thank the anonymous referee for valuable suggestions and corrections that have helped to improve the clarity of the presentation.

APPENDIX A: IMPLEMENTATION NOTES

A1 Truncation error analysis for a smooth high Mach number flow

This section presents a detailed error analysis of the evolution of the Hubble-type diverging flow, see sections 3.2 and 5.1. We are particularly interested in the consequences of neglecting the difference between the cell average and cell centred values of conserved quantities. As we show below, this leads to a secular error in the evolution of the internal energy so that it becomes negative. The error is first order in time and second order in space, independent of the actual order of discretisation of the scheme in space and time. This means that lowering the time step does not diminish the error; only by significantly increasing the spatial resolution can the error be reduced.

Firstly, we verify that solution (12) satisfies the conservation laws:

$$\frac{\partial \rho}{\partial t} = -\frac{v'_0 \rho_0}{(1+v'_0 t)^2} = -\frac{\partial(\rho v)}{\partial x}, \quad (\text{A1})$$

$$\frac{\partial(\rho v)}{\partial t} = -\frac{2\rho_0 v_0'^2 x}{(1+v'_0 t)^3} = -\frac{\partial(\rho v^2)}{\partial x}, \quad (\text{A2})$$

$$\frac{\partial u_g}{\partial t} = -\frac{\Gamma u_0 v'_0}{(1+v'_0 t)^{\Gamma+1}} = -\frac{\partial[(u_g + p_g)v]}{\partial x}, \quad (\text{A3})$$

so the system (12) correctly describes the time evolution of the initial distribution described by setting $t = 0$ in the system.

Let us assume that the spatial reconstruction on the primitive quantities is exact but one does not take into account the difference between cell averaged and cell centred values of conserved quantities. We use the Euler method to discretise time stepping and check if the method converges at second order in time as one would naively expect. We only need to consider the first time step since for all successive time steps the result of the previous time step(s) can be considered an initial condition. We define a uniform numerical grid consisting of grid cells $\Delta_i = [x_{i-1/2}, x_{i+1/2}]$ of size h . For spatial discretisation we use the simplest finite volume scheme: we linearly interpolate the values of primitive quantities from cell centres to cell interfaces within each of the grid cells. Since in the above solution all primitive variables depend linearly on x , this linear interpolation is exact.

Consider the i th grid cell, Δ_i . For clarity we shall omit the index i where it does not lead to confusion. Let us integrate the equations from $t = 0$ to $t = \Delta t$. The conserved variables are the density ρ , specific momentum $p = \rho v$, and the total specific energy $E = \rho v^2/2 + u_g$. The discretisation of conservation laws then takes the form:

$$\begin{aligned} \Delta\langle\rho\rangle &= -\Delta t [\rho_0 v'_0(x+h/2) - \rho_0 v'_0(x-h/2)]/h \\ &= -\rho_0 v'_0 \Delta t, \end{aligned} \quad (\text{A4})$$

$$\begin{aligned} \Delta\langle p\rangle &= -\Delta t [\rho_0 v_0'^2(x+h/2)^2 - \rho_0 v_0'^2(x-h/2)^2]/h \\ &= -2\rho_0 v_0 v_0' \Delta t, \end{aligned} \quad (\text{A5})$$

$$\begin{aligned} \Delta\langle E\rangle &= -\Delta t [\rho_0 v_0'^3(x+h/2)^3/2 - \rho_0 v_0'^3(x-h/2)^3/2]/h \\ &\quad -\Delta t (u_g + p_g)_0 v_0' \\ &= -(\rho v^2/2)_0 3v_0' \Delta t (1 + 1/12 h^2/x^2) - (u_g + p_g)_0 v_0' \Delta t, \end{aligned} \quad (\text{A6})$$

where angle brackets indicate averaging over the grid cell

and index ‘0’ indicates values taken at $t = 0$. The latter equation corresponds to the following conservation law:

$$\frac{\partial E}{\partial t} = -\frac{\partial}{\partial x} [(E + P)v] \equiv -\frac{\partial}{\partial x} [\rho v^3/2 + (u_g + p_g)v]. \quad (\text{A7})$$

The above expressions (A4) – (A6) are so far exact up to first order in time. Now suppose we remove the angle brackets on the l.h.s. in the above expressions, i.e. do not make a distinction between cell centred and cell averaged quantities. Equations (A4) and (A5) will still be exact up to first order in time for the particular problem considered, i.e. they will still give the updates to cell centred quantities ρ and p that are first order accurate in time. This is because ρ and $p = \rho v$ are linear functions of x and thus their average value in any grid cell is the same as the point value at the cell centre. This is not the case, however, for equation (A6) where energy E is a nonlinear function of x : $E \neq \langle E \rangle$. This also can be seen from the expansion of equation (12), according to which the cell centred conserved quantities evolve according to

$$\begin{aligned} \Delta \rho &= \rho_0 (-v'_0 \Delta t + v_0'^2 \Delta t^2 - \dots), \\ \Delta p &= p_0 (-2v'_0 \Delta t + 3v_0'^2 \Delta t^2 - \dots), \\ \Delta E &= (\rho v^2/2)_0 (-3v'_0 \Delta t + 6v_0'^2 \Delta t^2 - \dots) \\ &\quad + (u_g + p_g)_0 (-v'_0 \Delta t + (\Gamma + 1)v_0'^2 \Delta t^2/2 - \dots). \end{aligned} \quad (\text{A8})$$

So, by treating the update to the average of the energy in the grid cell as the update to the point value of energy, we are making an absolute error in ΔE equal to

$$\mathcal{E}(\Delta E) = \Delta \langle E \rangle - \Delta E = -\frac{1}{8} \rho_0 v_0'^2 v_0' h^2 \Delta t \frac{h^2}{x^2} \equiv -\frac{1}{8} \rho_0 v_0'^3 h^2 \Delta t. \quad (\text{A9})$$

Note that up to first order in time, $\mathcal{E}(\Delta \rho) = \mathcal{E}(\Delta p) = 0$. Since the internal energy is computed from the values of conserved quantities via

$$u_g = E - p^2/(2\rho), \quad (\text{A10})$$

the error in the update to internal energy is

$$\mathcal{E}(\Delta u_g) = \mathcal{E}(\Delta E) = -\frac{1}{8} \rho_0 v_0'^2 h^2 v_0' \Delta t. \quad (\text{A11})$$

It is first order in time for every step, which means that using smaller steps (i.e. lowering the Courant factor) does not lead to convergence. We note that using higher order discretisation in time and/or space does not help to avoid this error. If we were to use a higher order time stepping discretisation scheme, the time stepping error would remain the same because higher order time stepping schemes assume that each simple first order time step is accurate to first order. However, here this is not the case. So for higher order time stepping error (A11) remains the same. Only by increasing the spatial resolution can one get convergence of second order in space, independent of the actual spatial and temporal order of approximation of the scheme.

We can estimate the error in the internal energy at a characteristic time of the evolution by setting $\Delta t = 1/v_0'$,

$$\frac{\mathcal{E}(\Delta u_g)}{u_0} \Big|_{v_0' \Delta t = 1} \sim -\frac{\rho_0 v_0'^2 h^2}{u_0} \sim -M_{\min}^2. \quad (\text{A12})$$

This error is on the order of the minimum of the Mach number on the grid squared. Therefore, for large Mach numbers, the schemes that do not take into account the difference between the point and average values of conserved quantities

Table A1. Optimal weights for various types of WENO-5 reconstruction. According the convention of Shu (1997) adopted in this paper, d_0 , d_1 , and d_2 are the right, central, and left optimal weights.

Reconstruction type	d_0	d_1	d_2
Centre to left face	1/16	5/8	5/16
Centre to right face	5/16	5/8	1/16
Average to centre	-9/80	49/40	-9/80
Centre to average	-17/240	137/120	-17/240

make very large errors in the evolution of the internal energy and require the use of the resolution proportional to the Mach number of the flow in order to correctly capture the evolution of the internal energy. For instance, for a Mach number $M_{\min} = 100$, the resolution has to be increased by about two orders of magnitude. See section 5.1 for a numerical verification of these results.

A2 Reconstruction matrices and optimal weights for WENO-5

In WENO-5 the integer k in section 4.5 is equal to three. Thus we have 3 stencils, each of length 3. The reconstruction matrices in equation (18) for average to centre and centre to average reconstructions, $c_{ij}^{(\text{ac})}$ and $c_{ij}^{(\text{ca})}$, are the inverse of each other:

$$\begin{aligned} c_{ij}^{(\text{ac})} &= \begin{pmatrix} 23/24 & 1/12 & -1/24 \\ -1/24 & 13/12 & -1/24 \\ -1/24 & 1/12 & 23/24 \end{pmatrix}, \\ c_{ij}^{(\text{ca})} &= \begin{pmatrix} 25/24 & -1/12 & 1/24 \\ 1/24 & 11/12 & 1/24 \\ 1/24 & -1/12 & 25/24 \end{pmatrix}. \end{aligned}$$

The reconstruction matrices for centre to left interface and centre to right interface reconstructions, $c_{ij}^{(\text{cl})}$ and $c_{ij}^{(\text{cr})}$, are:

$$\begin{aligned} c_{ij}^{(\text{cl})} &= \begin{pmatrix} 15/8 & -5/4 & 3/8 \\ 3/8 & 3/4 & -1/8 \\ -1/8 & 3/4 & 3/8 \end{pmatrix}, \\ c_{ij}^{(\text{cr})} &= \begin{pmatrix} 3/8 & 3/4 & -1/8 \\ -1/8 & 3/4 & 3/8 \\ 3/8 & -5/4 & 15/8 \end{pmatrix}. \end{aligned}$$

The optimal weights for centre to edge, average to centre, and centre to average reconstructions can be computed by equating the expressions (19) and (20). For completeness, we give them here, see table A1. Note that for average to centre and centre to average reconstructions, negative optimal weights appear that require a special treatment. See section 4.7 for a discussion.

A3 Choosing the value of ϵ

The standard WENO weights computation procedure uses a fixed value of ϵ for the purpose of avoiding division by zero in (23) (Jiang & Shu 1996; Shu 1997). However, setting ϵ

to a constant value independent of the function being interpolated sets artificial, irrelevant scales for a problem. Any discontinuity in the interpolant, such that smoothness indicators for the stencils that cross that discontinuity are much smaller than ϵ , is mistakenly treated by the reconstruction as part of smooth flow.

Let us consider $\epsilon \ll 1$. Then a contact discontinuity, which is a density jump with $\Delta\rho = 1$ at $x = 0$,

$$\rho(x) = \begin{cases} 2, & x \geq 0 \\ 1, & x < 0, \end{cases} \quad (\text{A13})$$

is correctly treated by the reconstruction, i.e. the reconstruction avoids using the stencils that pass through the discontinuity. However, if the same density jump is recast in different density units,

$$\tilde{\rho}(x) = \begin{cases} 2\epsilon, & x \geq 0 \\ \epsilon, & x < 0, \end{cases} \quad (\text{A14})$$

it is not avoided by the reconstruction because in (23) $\epsilon \gg \beta_r \sim (\Delta\tilde{\rho})^2 \sim \epsilon^2$. The addition of ϵ to the smoothness indicators in this case effectively hides the jump from the reconstruction and leads to an oscillatory reconstruction.

We propose the following algorithm for the adaptive choice of ϵ . We leave the weights computation (23) – (24) the same but modify the smoothness indicators that come into it:

$$\beta'_r = \beta_r + \epsilon \|v^2\| + \delta, \quad (\text{A15})$$

where $\|v^2\|$ is the sum of v_i^2 within the WENO stencil and δ is the smallest positive number the floating-point type used in the numerical implementation of the method can hold; it is added to avoid division by zero when $\|v^2\|$ vanishes. We choose an ϵ such that it is larger than the relative machine precision in the computation of smoothness indicators and at the same time is negligible compared to them in shocks, $\epsilon = (c\epsilon_{\text{machine}})^2$. Here $\epsilon_{\text{machine}}$ is of order of relative machine precision for the float type used and c is a sufficiently large constant. We choose $c = 100$, so for *double precision* we have $\epsilon_{\text{machine}} \sim 10^{-15}$ and $\epsilon = 10^{-26}$.

Further, in order to extend the dynamic range of the reconstruction and avoid division by small numbers (smoothness indicators become small for small $\|v^2\|$), prior to plugging β'_r 's into the weights computation (23) we rescale them so that they add up to unity:

$$\beta''_r = \frac{\beta'_r}{\|\beta'_r\|}, \quad (\text{A16})$$

where $\|\beta'_r\| = \sum_{r=0}^{r=k-1} \beta'_r$.

Finally, we use the usual weights computation procedure (23) – (24) in which we use modified smoothness indicators β''_r (A16) and the value of ϵ determined above.

A4 At what order does WENO-5 actually converge in smooth flows?

Assuming we can neglect ϵ in the definitions of the weights, then in order to comply with (21) we need to have for $r = 0, \dots, k - 1$:

$$\beta_r = D \left[1 + \mathcal{O}(h^{k-1}) \right], \quad (\text{A17})$$

where D is a positive constant common to all stencils at a given resolution (so D may depend on the grid cell size, h).

Let us verify if for a smooth function $v(x)$ smoothness indicators (22) satisfy requirement (A17) for the case of WENO-5, i.e. $k = 3$. The smoothness indicators for cell centre to interface, average to centre, and centre to average reconstructions are the same for the case of WENO-5 (see appendix A6) and are given by:

$$\begin{aligned} \beta_0 &= \frac{1}{4}(-3v_i + 4v_{i+1} + v_{i+2})^2 + \frac{13}{12}(v_i - 2v_{i+1} + v_{i+2})^2, \\ \beta_1 &= \frac{1}{4}(v_{i+1} - v_{i-1})^2 + \frac{13}{12}(v_{i-1} - 2v_i + v_{i+1})^2, \\ \beta_2 &= \frac{1}{4}(v_{i-2} - 4v_{i-1} + 3v_i)^2 + \frac{13}{12}(v_{i-2} - 2v_{i-1} + v_i)^2. \end{aligned} \quad (\text{A18})$$

Using Taylor expansion, this can be cast into

$$\begin{aligned} \beta_0 &= \frac{1}{4}(2v'h - 2/3v'''h^3 - 1/4v^{(4)}h^4)^2 + \frac{13}{12}(v''h^2 + v'''h^3)^2, \\ \beta_1 &= \frac{1}{4}(2v'h + 1/3v'''h^3)^2 + \frac{13}{12}(v''h^2)^2, \\ \beta_2 &= \frac{1}{4}(2v'h - 2/3v'''h^3 + 1/4v^{(4)}h^4)^2 + \frac{13}{12}(v''h^2 - v'''h^3)^2, \end{aligned} \quad (\text{A19})$$

with the truncation error $\mathcal{O}(h^6)$. Here the derivatives are evaluated at the cell centre $x = x_i$: $v^{(n)} \equiv v^{(n)}(x_i)$. If $v' \neq 0$, then

$$\beta_r = (v'h)^2 [1 + \mathcal{O}(h^2)], \quad r = 0, 1, 2, \quad (\text{A20})$$

which satisfies (A17) and agrees with Jiang & Shu (1996). This means that if the v' -containing terms dominate in (A19), then the smoothness indicators give nearly optimal weights that satisfy (21), and hence the truncation order of WENO reconstruction (19) is $\mathcal{O}(h^{2k-1}) \sim \mathcal{O}(h^5)$.

However, at simple extrema with $v' = 0$ and $v'' \neq 0$, or more precisely with $|v'|h \ll |v'''|h^3 \ll |v''|h^2$, we have for smoothness indicators,

$$\beta_r = \frac{13}{12}(v''h^2)^2 [1 + 2(v'''/v'')h + \mathcal{O}(h^2)], \quad r = 0, 1, 2, \quad (\text{A21})$$

which means that neither (A17) nor (21) are satisfied, and WENO reconstruction (19) has a larger truncation error, $\mathcal{O}(h^{2k-2}) \sim \mathcal{O}(h^4)$, near the such extrema. This reduction in the order of the scheme occurs because the second derivative approximation in the smoothness indicators (A18) is only first order accurate. This disagrees with the result of Jiang & Shu (1996). They erroneously consider the numerical approximation to the 2nd derivative to be 2nd order accurate, i.e. they are missing the term proportional to v''' in (A21). Therefore in general the approximation order of the WENO-5 scheme at extrema reduces to 4, and only in the special case of extrema with $v''' = 0$ does WENO-5 give fifth order approximation, e.g. for $v(x) = \sin x$.

Finally, if both first and second derivatives become small compared to higher order ones (at a high order extremum, a critical point, or in a smooth region of the flow dominated by high-order derivatives) the order of the WENO-5 scheme reduces to the third one. This happens in contact discontinuities and leads to their excessive diffusion, this also happens near inflection points, e.g. of the $v(x) = x^3$ function: here WENO-5 is unable to capture the dependence near $x = 0$ exactly even though a fifth order polynomial would be able to.

A5 High order approximation in smooth monotonic flows

WENO-5 scheme aims to obtain the flattest reconstruction profile inside a grid cell of interest: it favors the stencils that minimize the absolute value of the first and second derivatives within the grid cell. In smooth flows that are locally well approximated by a parabola these derivatives do not change significantly between the stencils, so such a prescription leads to nearly optimal weights given to stencils and results in the fifth order of approximation. However, if any terms higher than second order ones are significant in the Taylor expansion of the function, the WENO-5 scheme reduces the reconstruction order down to the third one. This reduction leads to unwanted diffusion of contact discontinuities that becomes very large without the use of field-by-field decomposition.

To avoid such a reduction of the order of the scheme, we use a fifth order interpolation polynomial for reconstruction if the polynomial and its derivatives are monotonic. This minimizes the amount oscillation in the reconstructed solution and maintains a high order of interpolation in the monotonic regions of the flow. We use this approach for the centre to edge reconstruction. A similar idea is used in the PPM reconstruction procedure (Colella & Woodward 1984; Mignone et al. 2005).

Consider an exponential dependence $f(x) = e^x$ with the grid cell centres located at $x_i = hi$, $h = 1$. In this case the WENO-5 weights (24) are $(\omega_0, \omega_1, \omega_2) \propto (0.007d_0, 0.09d_1, 0.9d_2)$ independent of the value of i ; here d_r 's are the optimal weights (see text after equation (20)). WENO-5 is giving about 90% of the weight to one of the stencils, therefore the WENO-5 reconstruction order is effectively reduced from 5 to 3. In this case, the fifth order polynomial interpolation through, e.g., points x_{-2}, \dots, x_2 would have no oscillations at the interval $[x_{-1}, x_1]$ and could well be used.

Therefore, prior to applying the standard WENO-5 reconstruction inside an i th grid cell, we consider the fifth order reconstruction polynomial $f_5(x)$. It interpolates the set of discrete values f_{i-2}, \dots, f_{i+2} at points x_{i-2}, \dots, x_{i+2} . We check if all of the polynomial's derivatives are monotonic at the interval $[x_{i-1}, x_{i+1}]$ and if they are, we use this polynomial for interpolation instead of the WENO-5 interpolation. For a fifth order polynomial, it suffices to check that each of the first three derivatives, $f_5^{(n)}$, $n = 1, 2, 3$, has the same sign at both ends of the interval; below for compactness we shall omit the index '5'.

We now describe an indicator that vanishes unless the function values f_{i-2}, \dots, f_{i+2} form a monotonic sequence and the interpolation polynomial $f(x)$ and all of its derivatives are monotonic at (x_{i-1}, x_{i+1}) (in which case it is unity). In order to avoid switching between the schemes, we design the indicator to be a smooth function of discrete function values. We define the minimum value by absolute magnitude of an n th derivative at the interval, $f_{\min}^{(n)} = \text{MINMOD} [f^{(n)}(x_{i-1}), f^{(n)}(x_{i+1})]$. In order to ensure monotonicity of discrete values, we redefine $f_{\min}^{(1)} = \text{MINMOD} [f_{\min}^{(1)}, f_{i-1} - f_{i-2}, f_{i+2} - f_{i+1}]$. Finally, we compute the minimum absolute value of nondimensionalized derivatives of the reconstruction polynomial $f(x)$, $f_{\min}^{(\cdot)}$

$\min_{n=1, 2, 3} |f_{\min}^{(n)} h^n|$. We refer to the weight that we give to the fifth order polynomial reconstruction as the monotonicity indicator,

$$\alpha = \max \left\{ 0, \min \left[1, f_{\min}^{(\cdot)} / (\sqrt{\epsilon} \|f\| + \delta) \right] \right\}, \quad (\text{A22})$$

where $\|f\| = \sum_{j=i-2}^{i+2} |f_j|$ is the norm of $f(x)$ at the stencil and δ – added to avoid division by zero – is the minimum positive value that a floating-point variable can hold on our machine. In the above formula ϵ controls how fast the use of the fifth order polynomial for reconstruction kicks in when the function and its derivatives become monotonic. For consistency, we choose ϵ to be the same as the one in the WENO weights computation procedure (A15), (A16), (23), (24).

The reconstructed value we use is given by a linear combination of the fifth order accurate value of the polynomial, f_5 , and that of the WENO-type reconstruction, f_{WENO} :

$$f = \alpha f_5 + (1 - \alpha) f_{\text{WENO}}, \quad (\text{A23})$$

where we have returned back to the notation f_5 for denoting the fifth order reconstruction polynomial.

Since the reconstruction due to the fifth order polynomial is equivalent to the WENO-5 reconstruction with weights set to optimal ones, equation (A23) is equivalent to using the WENO-5 reconstruction with modified weights ω'_r :

$$\omega'_r = \alpha d_r + (1 - \alpha) \omega_r, \quad r = 0, \dots, k - 1. \quad (\text{A24})$$

This provides a smooth transition between using the polynomial and the WENO-type reconstructions.

A6 Higher order smoothness indicators

High order WENO-type schemes provide better convergence properties near critical points of smooth flows than their lower-order counterparts but have a higher computational cost (Qiu & Shu 2002). In this section we summarize the properties of higher order smoothness indicators. In particular, we concentrate on the convergence properties of WENO-type schemes near the critical points of smooth flows: when does a WENO- n scheme provide the maximal, n th, order of convergence?

One can show for any k (at least up to $k = 7$ as we have checked in Mathematica) that any smoothness indicator (22) can be cast in the form analogous to that of (A19): as a linear combination of the squares of discrete approximations to the derivatives at $x = x_i$. For instance for the case of $k = 4$, we

have for the smoothness indicators:

$$\begin{aligned} \beta_0 = & -\frac{1}{32}(-3v_i + 4v_{i+1} - v_{i+2})^2 \\ & + \frac{1}{32}(-11v_i + 18v_{i+1} - 9v_{i+2} + 2v_{i+3})^2 \\ & + \frac{13}{12}(2v_i - 5v_{i+1} + 4v_{i+2} - v_{i+3})^2 \\ & + \frac{3169}{2880}(-v_i + 3v_{i+1} - 3v_{i+2} + v_{i+3})^2, \end{aligned} \quad (\text{A25})$$

$$\begin{aligned} \beta_1 = & + \frac{1}{16}(v_{i+1} - v_{i-1})^2 \\ & + \frac{1}{48}(-2v_{i-1} - 3v_i + 6v_{i+1} - v_{i+2})^2 \\ & + \frac{13}{12}(v_{i-1} - 2v_i + v_{i+1})^2 \\ & + \frac{3109}{2880}(-v_{i-1} + 3v_i - 3v_{i+1} + v_{i+2})^2, \end{aligned} \quad (\text{A26})$$

$$\begin{aligned} \beta_2 = & + \frac{1}{16}(v_{i+1} - v_{i-1})^2 \\ & + \frac{1}{48}(v_{i-2} - 6v_{i-1} + 3v_i + 2v_{i+1})^2 \\ & + \frac{13}{12}(v_{i-1} - 2v_i + v_{i+1})^2 \\ & + \frac{3109}{2880}(-v_{i-2} + 3v_{i-1} - 3v_i + v_{i+1})^2, \end{aligned} \quad (\text{A27})$$

$$\begin{aligned} \beta_3 = & -\frac{1}{32}(v_{i-2} - 4v_{i-1} + 3v_i)^2 \\ & + \frac{1}{32}(-2v_{i-3} + 9v_{i-2} - 18v_{i-1} + 11v_i)^2 \\ & + \frac{13}{12}(-v_{i-3} + 4v_{i-2} - 5v_{i-1} + 2v_i)^2 \\ & + \frac{3169}{2880}(-v_{i-3} + 3v_{i-2} - 3v_{i-1} + v_i)^2. \end{aligned} \quad (\text{A28})$$

This is a much more conceivable representation of higher order smoothness indicators than the one used in Balsara & Shu (2000). In fact, this form allows one to easily prove the properties of higher order smoothness indicators the same way as we did for the case $k = 3$. Again, using Taylor expansion, we get:

$$\begin{aligned} \beta_0 = & -\frac{1}{8}\left(v'h - \frac{1}{3}v^{(3)}h^3 - \frac{1}{4}v^{(4)}h^4\right)^2 + \frac{9}{8}\left(v'h + \frac{1}{4}v^{(4)}h^4\right)^2 \\ & + \frac{13}{12}\left(v''h^2 - \frac{11}{12}v^{(4)}h^4\right)^2 + \frac{3169}{2880}\left(v^{(3)}h^3 + \frac{3}{2}v^{(4)}h^4\right)^2, \end{aligned} \quad (\text{A29})$$

$$\begin{aligned} \beta_1 = & + \frac{1}{4}\left(v'h + \frac{1}{6}v^{(3)}h^3\right)^2 + \frac{3}{4}\left(hv' - \frac{1}{12}h^4v^{(4)}\right)^2 \\ & + \frac{13}{12}\left(v''h^2 + \frac{1}{12}v^{(4)}h^4\right)^2 + \frac{3109}{2280}\left(v^{(3)}h^3 + \frac{1}{2}h^4v^{(4)}\right)^2, \end{aligned} \quad (\text{A30})$$

$$\begin{aligned} \beta_2 = & -\frac{1}{4}\left(v'h + \frac{1}{6}v^{(3)}h^3\right)^2 + \frac{3}{4}\left(v'h + \frac{1}{12}v^{(4)}h^4\right)^2 \\ & + \frac{13}{12}\left(v''h^2 + \frac{1}{12}v^{(4)}h^4\right)^2 + \frac{3109}{2880}\left(v^{(3)}h^3 - \frac{1}{2}h^4v^{(4)}\right)^2, \end{aligned} \quad (\text{A31})$$

$$\begin{aligned} \beta_3 = & -\frac{1}{8}\left(v'h - \frac{1}{3}v^{(3)}h^3 + \frac{1}{4}v^{(4)}h^4\right)^2 + \frac{9}{8}\left(v'h - \frac{1}{4}h^4v^{(4)}\right)^2 \\ & + \frac{13}{12}\left(v''h^2 - \frac{11}{12}h^4v^{(4)}\right)^2 + \frac{3169}{2880}\left(v^{(3)}h^3 - \frac{3}{2}h^4v^{(4)}\right)^2, \end{aligned} \quad (\text{A32})$$

with the truncation error of $\mathcal{O}(v'h^6) + \mathcal{O}(v''h^7) + \mathcal{O}(h^8)$.

If $v' \neq 0$, we get the analog of equation (A20),

$$\beta_r = (v'h)^2 [1 + \mathcal{O}(h^2)], \quad r = 0, 1, 2, 3; \quad (\text{A33})$$

further, for $v' = 0$, $v'' \neq 0$ we obtain the analog of equation (A21),

$$\beta_r = 13/12(v''h^2)^2 [1 + \mathcal{O}(h^2)], \quad r = 0, 1, 2, 3. \quad (\text{A34})$$

This shows that the smoothness indicators for WENO-7 (with $k = 4$) are capable of handling the extrema, where $v' = 0$, without any reduction in order: the order of the scheme is then $\mathcal{O}(h^{2k-1}) \sim \mathcal{O}(h^7)$. However, when both $v' = 0$ and $v'' = 0$,

$$\beta_r = 1043/960(v^{(3)}h^3)^2[1 + \mathcal{O}(h)], \quad r = 0, 1, 2, 3, \quad (\text{A35})$$

so the order of the scheme reduces to $\mathcal{O}(h^{2k-2}) \sim \mathcal{O}(h^6)$ for this case.

More generally, consider a WENO-($2k - 1$) scheme, which uses stencils of length k . As can be verified for each particular k , the numerical approximations to $v', \dots, v^{(k-2)}$, that the smoothness indicators are comprised of, have truncation errors that do not contain any terms proportional to $v', \dots, v^{(k-2)}$. Therefore, in analogy with the above discussion of the $k = 3$ and $k = 4$ cases, the WENO scheme that uses stencils of length k can be shown to be able to handle the maxima without reducing the reconstruction order if at least one of the 1st, 2nd, \dots , $(k - 2)$ th derivatives at $x = x_i$ is nonzero.

Note that for $k \leq 3$ the smoothness indicators are the same for all reconstruction types: average to interface, $\langle v \rangle_i \rightarrow v_{i+1/2}$, cell centre to interface, $v_i \rightarrow v_{i+1/2}$, average to centre, $\langle v \rangle_i \rightarrow v_i$, and centre to average, $v_i \rightarrow \langle v \rangle_i$, reconstructions and are given by equations (A18). This is because for $k \leq 3$ the difference between cell centre and cell average values is the same for all points in the stencil. However, for larger k , this difference starts to vary from point to point within the stencil, and for $k \geq 4$ the smoothness indicators become different for these types of reconstruction. So, the 4th order smoothness indicators presented here for cell centre to interface, $v_i \rightarrow v_{i+1/2}$, reconstruction are different from the smoothness indicators given by Balsara & Shu (2000) for the average to interface, $\langle v \rangle_i \rightarrow v_{i+1/2}$, reconstruction.

A7 Algorithm for reducing the stencil size

WENO schemes only operate on stencils of a fixed length and this length is the smallest the stencils can get (e.g., it is 3 for the case of WENO-5). There are several cases when there may not be large enough smooth region for a stencil of a large size to fit in, e.g. (1) for a reconstruction between two shocks that are about to interact, (2) in the case of a state that has to be ‘built-up’, and (3) for the grid cells inside unresolved discontinuities (Harten et al. 1987).

We have developed an algorithm of adaptive reduction of the stencil size: the algorithm locates the grid cells inside sharp discontinuities in the flow, and a lower-order WENO-3 reconstruction (Shu 1997) is used there. In this algorithm we do not rely on the pressure jumps (as is done in the PPM algorithm, see, e.g., Colella & Woodward 1984) as indicators of shocks because in the supersonic regime, where the pressure is negligible and, possibly, noisy, this approach may lead to excessive reduction of the order of the scheme.

The information about the discontinuities in the flow is actually encoded in the weights (23) used by the WENO reconstruction. For the purposes of the stencil reduction algorithm described below, we compute the unoptimized weights that are obtained by setting $d_r = 1$ in (23), which, given the smoothness indicators, is a fast computation. We want to find out if we need to reduce the order of reconstruction

for the i th grid cell and we are using the WENO-5 scheme with $k = 3$. Suppose, the weight ω_0^i is very large compared to ω_2^{i+2} , i.e. the flow around the i th cell has a steeper profile than that near the $(i + 2)$ nd cell. This is an indication that the i th cell is located inside a discontinuity, so we use the lower-order WENO-3 reconstruction there (Shu 1997). Namely, for i th grid cell we define the ratio

$$\mathcal{R} = \mathcal{F} \left(\frac{\omega_0^i}{\omega_2^{i+2}}, \frac{\omega_2^i}{\omega_0^{i-2}} \right), \quad (\text{A36})$$

where we choose function \mathcal{F} below depending on the reconstruction type, and define the fraction of the WENO-3 reconstruction that we use in that grid cell as

$$\alpha_3 = \max \left[0, \min \left(\frac{\mathcal{R} - \mathcal{R}_{\min}}{\mathcal{R}_{\max} - \mathcal{R}_{\min}}, 1 \right) \right], \quad (\text{A37})$$

so the fraction of the WENO-5 reconstruction is $(1 - \alpha_3)$. This means that for the ratios of weights $\mathcal{R} < \mathcal{R}_{\min}$ we fully use the WENO-5 reconstruction procedure, for $\mathcal{R} > \mathcal{R}_{\max}$ we fully use the WENO-3 one, and linearly transition between them for intermediate \mathcal{R} . For the cell centre to interface reconstruction we use $\mathcal{F}(x, y) = \max(x, y)$, $\mathcal{R}_{\min} = 1.3$, and $\mathcal{R}_{\max} = 1.6$. This provides reduction in the order of reconstruction in unresolved discontinuities whose width is smaller than about the stencil size (5 points for WENO-5) and avoids reduction in the kinks of the flow (discontinuities in first derivative). For centre to average and average to centre reconstructions we use $\mathcal{F}(x, y) = \min(x, y)$, $\mathcal{R}_{\min} = 10$, and $\mathcal{R}_{\max} = 15$. This allows reduction in unresolved discontinuities and in the kinks of the flow. Lastly, the stiff relativistic regime where the effective Lorentz factor $\gamma_{\text{eff}} \equiv \gamma(\rho + u_g + p_g)/\rho \geq 10$ stresses higher-order methods since, unlike with TVD methods, the interpolated value can lie outside of the range given by the surrounding values. To avoid mild oscillations in the ultrarelativistic test in section 5.19, we use the latter reduction method for all reconstructions if $\gamma_{\text{eff}} \geq 10$. This helps by keeping the interpolations consistent with each other and only makes a mild difference near the shock in this single ultrarelativistic test.

In smooth flows where the first and second derivatives do not vary much from grid cell to grid cell WENO-5 maintains high order accuracy: all weights are on the order of 1/3, and the reduction does not operate. However, if there is a discontinuity in the flow, the weights for the points that are near it will vanish for the stencils crossing the discontinuity, so a lower order reconstruction will be used for the points inside of the discontinuity. Similar to what is done in the flattening algorithm used by PPM (Colella & Woodward 1984; Mignone et al. 2005), we additionally reduce the order near shocks but avoid such a reduction near contact discontinuities. For each grid cell we modify α_3 as follows:

$$\alpha_3 = \max(\alpha_3, \mathcal{S}_i \alpha_{3,i-1}, \mathcal{S}_i \alpha_{3,i+1}), \quad (\text{A38})$$

where $\alpha_{3,i\pm 1}$ are the unmodified values of α_3 at the grid cells adjacent to the i th one and \mathcal{S}_i is an indicator of the shock strength that vanishes for no shock and becomes unity for a strong shock:

$$\mathcal{S}_i = \max \left[0, \min(1, 4\tilde{\mathcal{S}}_i - 1) \right], \quad (\text{A39})$$

$$\tilde{\mathcal{S}}_i = \frac{\rho_i \Delta |u^t(1 + u_t)| + \Delta |(p_g + u_g)u^t u_t + p_g|}{[\rho u^t(1 + u_t) + (p_g + u_g)u^t u_t + p_g]_i}. \quad (\text{A40})$$

$\tilde{\mathcal{S}}_i$ has the meaning of the relative jump in the energy ($-T^t_i - \rho u^t$), eq. (7), and $\Delta q = q_{i+1} - q_{i-1}$.

We introduce *reduced* WENO-5 weights, $\tilde{\omega}_r = (1 - \alpha_3)\omega_r$, and rewrite the reconstruction result,

$$f^{\text{WENO}} = \tilde{f}_5 + \tilde{\alpha}_3 f_3, \quad (\text{A41})$$

where \tilde{f}_5 is the reconstruction due to WENO-5 with the reduced weights, f_3 is the reconstructed value due to the WENO-3, and $\tilde{\alpha}_3 = 1 - \sum_r \tilde{\omega}_r$. We will modify the reduced WENO-5 weights in the following paragraph.

We perform the integration of source terms in the usual component-by-component way. However, we have to be more careful for average to centre and centre to average reconstructions since they operate on the conserved quantities. The difference between cell averaged and cell centred values cannot be treated in a pure component-by-component way because of the nonlinear coupling between the conserved quantities. For example, we would like to avoid using different stencils in average to centre reconstructions for total conserved energy and components of the total conserved momentum. For the conserved quantities we separately perform the reconstruction of the energy component in the way described in the previous paragraph. For each of the other components we modify the reduced WENO-5 weights to be equal to the minimum of the reduced WENO-5 weights for the energy component and ten times the WENO-5 weights for that component. This way in smooth regions for the reconstruction of all conserved quantities we use a common set of weights computed for the total conserved energy. Similarly, for the centre to average reconstruction of fluxes in i th direction, we use the same procedure as described above for the conserved quantities, but instead of using a common set of weights computed for the energy component, we use a common set of weights computed for the flux of i th component of momentum in the i the direction.

We make the reconstruction even more robust by reducing its order in non-smooth features of the flow that we refer to as cusps (defined below). Further, if there is a cusp in the γ -factor of the flow in a grid cell and cell to cell change of γ is larger than 1%, we do not perform the centre to average reconstruction of the fluxes whose values depend on the reconstruction of γ that has the cusp (since in this case the fluxes, which are steep functions of γ , are not smooth). We now explain what we mean by a cusp. Define $f'_{i+1/2} = f_{i+1} - f_i$, $f''_i = f'_{i+1/2} - f'_{i-1/2}$. First, consider the case of an increasing function, $f'_{i-1/2} > \sqrt{\epsilon} \|f\|$; we later will generalize the procedure. We then define a point i to be in a cusp if it is located between an inflection point (i.e., $f''_{i-1} > \sqrt{\epsilon} \|f\|$ and $f''_i < -\sqrt{\epsilon} \|f\|$) and a local maximum with one-sided derivatives different by no more than 50% by absolute value (i.e. either $4|f'_{i+1/2} + f'_{i-1/2}| < |f'_{i+1/2}| + |f'_{i-1/2}|$ or $4|f'_{i+3/2} + f'_{i-1/2}| < |f'_{i+3/2}| + |f'_{i-1/2}|$). In general, we define the function to contain the cusp at the point i if either the above is true or if it becomes true after the flip of the function sign, grid direction, or both. For consistency, we choose ϵ to be the same as the one in the WENO weights computation procedure (A15), (A16), (23), (24).

A8 Failsafe integration

As in other codes (Zhang & MacFadyen 2006; Gammie et al. 2003), we implement certain safety fea-

tures that enable our code to succeed in especially stiff regimes. In relativistic flows, there are states of conserved quantities (6) for which there exists no corresponding set of primitive quantities (10) at all. Further, a change in conserved quantities of less than 1% may correspond to an *infinite* change in primitive quantities. Therefore, any reconstruction operations directly performed on the conserved quantities or on the fluxes may in principle lead to unphysical states or instabilities. This is the reason why we carry out the crucial cell centre to interface reconstruction Step i (see section 3.6) on the primitive quantities instead of conserved quantities or fluxes: this guarantees that we always obtain a physically meaningful state at the interface and, therefore, a physically meaningful flux. However, the update to the conserved quantities due to this flux may sometimes lead to an unphysical state with a negative internal energy or density, or, as explained above, the corresponding state of primitive quantities may not at all exist. Here we describe the procedure that we follow in such cases in order to make the integration failsafe.

In our scheme the de-averaging and averaging reconstructions, Step iii and Step vii (see section 3.6), change the representation of conserved quantities but do not alter the locations of those. We avoid using the average to centre reconstruction if it makes a large difference for the total energy density in the fluid frame, $(\rho + u_g)$ in the hydrodynamic case we consider in this paper. In particular, we make sure that the primitive quantities \mathbf{p}_c , that correspond to cell centred conserved quantities, are not very different from \mathbf{p}_a , that correspond to cell averaged conserved quantities: we use \mathbf{p}_c if its difference from \mathbf{p}_a in the value of energy density in the fluid frame is smaller than 5%, use \mathbf{p}_a if that difference is larger than 10%, and linearly transition between these two values for an intermediate difference. If no primitive state \mathbf{p}_c has been found by the inversion, we use \mathbf{p}_a . This locally lowers the order of the scheme in stiff regimes where operations on the conserved quantities are not safe, so there our scheme becomes equivalent to the schemes that do not distinguish between the average and point values. Note, that this procedure does not affect the asymptotic order of convergence of the scheme since the difference between the cell averaged and cell centred values is $\mathcal{O}(h^2)$.

Occasionally, during the evolution negative rest-mass density or internal energy might occur. If a negative rest-mass density (internal energy) implies an imaginary sound speed, we set the sound speed to unity (zero) and continue the evolution. This adjustment of the sound speed only affects the diffusive flux used in the approximate HLL Riemann solver. Most of such negative rest-mass density and internal energy occurrences are due to inaccuracy of trial Runge-Kutta time steps and do not appear on the final Runge-Kutta time steps. Such behaviour is acceptable since at the end we get a high order accurate answer, and it does not matter that some of the intermediate steps that lead to this answer were unphysical. For the same reason we allow negative internal energy/baryon densities to occur at the final Runge-Kutta time steps. The idea is the same: to temporarily allow the solution to go out of the physical states space with the hope of it finally reaching a well-defined accurate state. For instance, negative internal energy/baryon densities may occur in front of a strong shock, however, we find that once the shock passes through, all of the states that

were temporarily unphysical are well-defined. Lastly, we implement a minor diffusive correction to the internal energy under special circumstances in order to improve the fidelity of the internal energy near shocks (as for a few cells near the shock in the caustic test in section 5.3). If the internal energy is negative but all surrounding values are larger, then the internal energy is considered to be an isolated failure and its value is chosen to be the smallest of the surrounding values in a way that leads to a symmetric result in multiple dimensions.

Finally, we apply some diffusive corrections to the primitive quantities used to obtain the flux. In rare cases that no state of primitive quantities can be found that corresponds to the state of the conserved quantities (i.e. an inversion from conserved to primitive quantities does not exist) we use the average of the existing surrounding states of the primitive quantities. This situation occurred only twice in the two-dimensional relativistic Riemann problem (section 5.20) in the highly relativistic part of the flow ($\gamma \approx 25$) and did not occur in any other test problems we have performed. If for all surrounding grid cells no primitive states can be found, we use the average of states of primitive quantities in the surrounding grid cells from the previous time step.

Note that the above features only alter the state of primitive quantities that are used in order to compute interface fluxes, therefore, the scheme remains conservative since the values of the conserved quantities are affected only through the fluxes.

A9 Catastrophic cancellation in nonrelativistic problems

In order to be able to successfully study both highly relativistic and nonrelativistic problems and avoid being severely limited by finite numerical precision⁹, we have to use the a special technique for performing the rest-mass subtraction in (7) and (8). For instance, in the calculation of conserved quantities from the primitive ones, given a 4-velocity u^μ , we need to find the kinetic energy, i.e. the difference between the total bulk motion energy and the rest-mass energy in the coordinate basis frame,

$$\rho u^t(-u_t - 1). \quad (\text{A42})$$

A similar procedure is followed in Aloy et al. (1999) for the special relativistic equations of motion. Further, the inverse process of computing the primitive quantities from conserved quantities involves computing a similar expression

$$\rho\gamma(\gamma - 1). \quad (\text{A43})$$

For nonrelativistic flows the value of γ may get so close to unity that within machine precision its numerical value is 1.0. This is why we cannot simply plug in such a value for γ in the above formula to compute the kinetic energy. For double precision, this happens for 3-velocity values of $v \lesssim 10^{-8}$. We alleviate the above problem by rewriting part

⁹ Even though we normally use the code at double precision, we have made it capable of performing computations at long double precision. For this, we use the long double versions of exponential, trigonometric, etc., functions from Cephes Math Library Release 2.7 and use the `-long_double` option for the Intel compiler.

of expression (A43) for kinetic energy with the help of the velocity information:

$$\gamma - 1 = \frac{1 - \sqrt{1 - v^2}}{\sqrt{1 - v^2}} = \frac{\gamma v^2}{1 + \sqrt{1 - v^2}} = \frac{\gamma^2 v^2}{1 + \gamma}, \quad (\text{A44})$$

where the final expression does not contain catastrophic cancellations and due to the particular choice of frame the Lorentz factor has the conventional form $\gamma = (1 - v^2)^{-1/2}$ (Noble et al. 2006).

In equation (A42) we can similarly rewrite the problematic part as follows:

$$-u_t - 1 = -g_{tt}u^i + 2\phi \frac{1 - g_{tt}}{1 + \hat{\gamma}} + \frac{\hat{\gamma}^2 \hat{v}^2}{1 + \hat{\gamma}}, \quad (\text{A45})$$

where $\hat{\gamma} = -g_{tt}u^t$ and $\hat{v}^2 = 2g_{it}v^i - 2\phi + g_{ij}v^i v^j$ play the roles of the γ -factor and the square of the velocity, $\phi = -(1 + g_{tt})/2$ is the gravitational potential and is small compared to unity for problems involving nonrelativistic gravity, so for such problems we separately store its value. Similarly, we separately compute and store the value of $(g^{tt} - 1)$, which appears when converting the total energy with rest-mass subtracted from the lab frame to the normal observer frame (Noble et al. 2006; Mignone & McKinney 2007).

The general expression (A45) avoids catastrophic cancellations both for relativistic problems and for problems involving nonrelativistic velocities and gravitational fields. We use this expression when computing the conserved quantities from the primitive ones as well as for the inverse process. Since expression (A45) is written in an arbitrary frame, it involves two additional terms as compared to (A44): the first one appears for a metric that has space-time mixing, the second one is due to a nonzero gravitational potential, and the third one corresponds to (A44).

A10 Catastrophic cancellation in ultrarelativistic problems

For the ultrarelativistic regime one can show that the inversion method we use (Mignone & McKinney 2007) that converts conserved to primitive quantities leads to well-defined relative errors in the primitive quantities for a machine accurate set of conserved quantities. In the ultrarelativistic hydrodynamic case, for a conserved lab-frame energy density (E), conserved mass density (D), and conserved momentum density (P^α), the Lorentz factor is given by

$$\gamma = \frac{E}{\sqrt{E^2 - P^2}}, \quad (\text{A46})$$

which can be used to obtain the rest-mass density

$$\rho = \frac{D}{\gamma}, \quad (\text{A47})$$

the relative 4-velocity

$$\tilde{u}^\alpha = \gamma \tilde{v}^\alpha = \gamma \frac{P^\alpha}{E}, \quad (\text{A48})$$

and the quantity $\chi \equiv u_g + p_g$,

$$\chi = \frac{E}{\gamma^2} - \frac{D}{\gamma}, \quad (\text{A49})$$

which with an equation of state can be used to determine both u_g and p_g . For this inversion we have neglected the term in the energy equation proportional to p_g compared to

$\gamma^2(\rho + \chi)$ and below we state how this limits the remaining arguments.

Given E , P , and D with an accuracy limited by a machine error of $\epsilon_{\text{machine}}$, one can show that the relative errors in primitive quantities are given by

$$\frac{d\gamma}{\gamma} \sim \left(\frac{\gamma}{\gamma_{\text{max}}}\right)^2 \equiv \epsilon_{\text{machine}} \gamma^2, \quad (\text{A50})$$

$$\frac{dv^\alpha}{v^\alpha} \sim \epsilon_{\text{machine}}, \quad (\text{A51})$$

$$\frac{d\chi}{\chi} \sim \left(\frac{\rho + \chi}{\chi}\right) \left(\frac{\gamma}{\gamma_{\text{max}}}\right)^2, \quad (\text{A52})$$

$$\frac{d\rho}{\rho} \sim \frac{d\gamma}{\gamma}. \quad (\text{A53})$$

These error estimates are valid as long as

$$\frac{\gamma}{\gamma_{\text{max}}} \gg \left(\frac{\chi}{\rho \gamma_{\text{max}}^2}\right)^{1/4}. \quad (\text{A54})$$

This implies a smaller than order unity error for the primitive quantities when

$$\gamma \lesssim \gamma_{\text{max}} \equiv \epsilon_{\text{machine}}^{-1/2}, \quad (\text{A55})$$

$$\chi \gtrsim \chi_{\text{min}} \equiv \frac{\rho(\gamma/\gamma_{\text{max}})^2}{1 - (\gamma/\gamma_{\text{max}})^2}, \quad (\text{A56})$$

and the error in ρ only sets the maximum allowed γ . For example, using double precision on a 32-bit machine gives conserved quantities that have at best a relative error of $\epsilon_{\text{machine}} \approx 2.2 \times 10^{-16}$ giving

$$\gamma_{\text{max}} = 6.7 \times 10^7. \quad (\text{A57})$$

For example, the ultrarelativistic test discussed in Aloy et al. (1999) (see section 5.19) with $\gamma = 2.24 \times 10^5$ and $p = 7.63 \times 10^{-6}$ for $\Gamma = 4/3$ gives $\chi \gtrsim \chi_{\text{min}}$, so their test is at the limit of resolving the pre-shock pressure for double precision. The post-shock region will be resolved as long as the pre-shock Lorentz factor is resolved.

Finally, an additional source of error can be incurred when an iterative inversion method uses the expression

$$\gamma = (1 - v^2)^{-1/2}, \quad (\text{A58})$$

as compared to

$$\gamma = \sqrt{1 + \tilde{u}^2}, \quad (\text{A59})$$

since repeated use of the prior expression leads to a cumulated catastrophic errors not present when using the latter expression. For this reason, in practice the GRMHD iterative solver of Noble et al. (2006) is limited to $\gamma \lesssim 10^5$ when using double precision.

REFERENCES

- Aloy M. A., Ibáñez J. M., Martí J. M., Müller E., 1999, *ApJS*, 122, 151
 Aloy M. A., Janka H.-T., Müller E., 2005, *A&A*, 436, 273
 Aloy M. A., Müller E., Ibáñez J. M., Martí J. M., MacFadyen A., 2000, *ApJ*, 531, L119
 Anderson M., Hirschmann E. W., Liebling S. L., Neilsen D., 2006, *Classical and Quantum Gravity*, 23, 6503
 Balbus S. A., Hawley J. F., 1991, *ApJ*, 376, 214

- Balsara D. S., Shu C.-W., 2000, *Journal of Computational Physics*, 160, 405
- Beskin V., Tchekhovskoy A., 2005, *A&A*, 433, 619
- Blandford R. D., Payne D. G., 1982, *MNRAS*, 199, 883
- Blandford R. D., Znajek R. L., 1977, *MNRAS*, 179, 433
- Blondin J., et al., 1991, VH-1 The Virginia Numerical Bull Session ideal hydrodynamics PPMLR, <http://wonka.physics.ncsu.edu/pub/VH-1/index.html>
- Blondin J. M., Lufkin E. A., 1993, *ApJS*, 88, 589
- Bondi H., 1952, *MNRAS*, 112, 195
- Bryan G. L., Norman M. L., Stone J. M., Cen R., Ostriker J. P., 1995, *Computer Physics Communications*, 89, 149
- Bucciantini N., Thompson T. A., Arons J., Quataert E., Del Zanna L., 2006, *MNRAS*, 368, 1717
- Colella P., Woodward P. R., 1984, *Journal of Computational Physics*, 54, 174
- De Villiers J.-P., Hawley J. F., 2003, *ApJ*, 589, 458
- De Villiers J.-P., Hawley J. F., Krolik J. H., 2003, *ApJ*, 599, 1238
- Del Zanna L., Bucciantini N., 2002, *A&A*, 390, 1177
- Feng L.-L., Shu C.-W., Zhang M., 2004, *ApJ*, 612, 1
- Fishbone L. G., Moncrief V., 1976, *ApJ*, 207, 962
- Font J. A., 2003, *Living Reviews in Relativity*, 6, 4
- Fryxell B., Olson K., Ricker P., Timmes F. X., Zingale M., Lamb D. Q., MacNeice P., Rosner R., Truran J. W., Tufo H., 2000, *ApJS*, 131, 273
- Gammie C. F., McKinney J. C., Tóth G., 2003, *ApJ*, 589, 444
- Gammie C. F., Shapiro S. L., McKinney J. C., 2004, *ApJ*, 602, 312
- Gardiner T. A., Stone J. M., 2005, *Journal of Computational Physics*, 205, 509
- Giacomazzo B., Rezzolla L., 2006, *J. Fluid Mech.*, 562, 223
- Goldreich P., Julian W. H., 1969, *ApJ*, 157, 869
- Ha Y., Gardner C. L., Gelb A., Shu C.-W., 2005, *J. Sci. Comput.*, 24, 597
- Harten A., 1983, *Journal of Computational Physics*, 49, 357
- Harten A., Engquist B., Osher S., Chakravarthy S. R., 1987, *Journal of Computational Physics*, 71, 231
- Hawley J. F., 2000, *ApJ*, 528, 462
- Hawley J. F., Wilson J. R., Smarr L. L., 1984, *ApJ*, 277, 296
- Hirose S., Krolik J. H., De Villiers J.-P., Hawley J. F., 2004, *ApJ*, 606, 1083
- Igumenshchev I. V., Narayan R., Abramowicz M. A., 2003, *ApJ*, 592, 1042
- Jiang G., Shu C.-W., 1996, *Journal of Computational Physics*, 126, 202
- Jiang G., Tadmor E., 1998, *SIAM Journal on Scientific Computing*, 19, 1892
- Koide S., 2003, *Phys. Rev. D*, 67, 104010
- Koide S., Shibata K., Kudoh T., Meier D. L., 2002, *Science*, 295, 1688
- Komissarov S. S., 2002, *MNRAS*, 336, 759
- Komissarov S. S., 2005, *MNRAS*, 359, 801
- Komissarov S. S., 2006, *MNRAS*, 367, 19
- Komissarov S. S., McKinney J. C., 2007, *MNRAS*, in press
- Krolik J. H., 1999, *Active galactic nuclei : from the central black hole to the galactic environment. Active galactic nuclei : from the central black hole to the galactic environment / Julian H. Krolik. Princeton, N. J. : Princeton University Press, c1999.*
- Landau L. D., Lifshitz E. M., 1975, *The classical theory of fields. Course of theoretical physics - Pergamon International Library of Science, Technology, Engineering and Social Studies*, Oxford: Pergamon Press, 1975, 4th rev.engl.ed.
- Latini M., Schilling O., Don W. S., 2007, *Journal of Computational Physics*, 221, 805
- Leismann T., Aloy M.-A., Müller E., 2004, *Ap&SS*, 293, 157
- LeVeque R. J., 1991, *Numerical Methods for Conservation Laws*. (Basel: Birkhäuser)
- Lewin W. H. G., van Paradijs J., van den Heuvel E. P. J., 1995, *X-ray binaries. Cambridge Astrophysics Series*, Cambridge, MA: Cambridge University Press, —c1995, edited by Lewin, Walter H.G.; Van Paradijs, Jan; Van den Heuvel, Edward P.J.
- Liska R., Wendroff B., 2003a, *Comparison of Several Difference Schemes on 1D and 2D Test Problems for the Euler Equations*, <http://www-troja.fjfi.cvut.cz/~liska/CompareEuler/compare8>
- Liska R., Wendroff B., 2003b, *SIAM Journal on Scientific Computing*, 25, 995
- Liu X.-D., Osher S., 1998, *Journal of Computational Physics*, 142, 304
- Lucas-Serrano A., Font J. A., Ibáñez J. M., Martí J. M., 2004, *A&A*, 428, 703
- Martí J. M., Müller E., 2003, *Living Reviews in Relativity*, 6, 7
- Marti J. M. A., Mueller E., Font J. A., Ibanez J. M. A., Marquina A., 1997, *ApJ*, 479, 151
- Mary I., Sagaut P., Deville M., 2000, *International Journal for Numerical Methods in Fluids*, 34, 371
- McKinney J. C., 2005, *ApJ*, 630, L5
- McKinney J. C., 2006a, *MNRAS*, 367, 1797
- McKinney J. C., 2006b, *MNRAS*, 368, 1561
- McKinney J. C., 2006c, *MNRAS*, 368, L30
- McKinney J. C., Gammie C. F., 2004, *ApJ*, 611, 977
- McKinney J. C., Narayan R., 2007a, *MNRAS*, 375, 513
- McKinney J. C., Narayan R., 2007b, *MNRAS*, 375, 531
- Mignone A., McKinney J. C., 2007, *MNRAS*, accepted (arXiv:0704.1679v1 [astro-ph]), 704
- Mignone A., Plewa T., Bodo G., 2005, *ApJS*, 160, 199
- Misner C. W., Thorne K. S., Wheeler J. A., 1973, *Gravitation*. San Francisco: W.H. Freeman and Co., 1973
- Mizuno Y., Nishikawa K.-I., Koide S., Hardee P., Fishman G. J., 2006, preprint (astro-ph/0609004)
- Morsony B. J., Lazzati D., Begelman M. C., 2006, preprint (astro-ph/0609254)
- Narayan R., McKinney J. C., Farmer A. J., 2007, *MNRAS*, 375, 548
- Noble S. C., Gammie C. F., McKinney J. C., Del Zanna L., 2006, *ApJ*, 641, 626
- Noelle S., Pankratz N., Puppo G., Natvig J. R., 2006, *Journal of Computational Physics*, 213, 474
- Noh W. F., 1987, *Journal of Computational Physics*, 72, 78
- Novikov I. D., Thorne K. S., 1973, In *Black Holes-Les Astres Occlus*, ed. C. De Witt & B. S. De Witt. New York: Gordon & Breach
- Phinney E. S., 1983, Ph.D. Thesis
- Press W. H., Teukolsky S. A., Vetterling W. T., Flannery B. P., 1992, *Numerical Recipes in C: The Art of Scientific*

- Computing. Cambridge University Press, New York, NY, USA
- Qiu J., Shu C.-W., 2002, *Journal of Computational Physics*, 183, 187
- Qiu J.-M., Shu C.-W., Feng L.-L., Fang L.-Z., 2006, *New Astronomy*, 12, 1
- Rahman T., Moore R. B., 2005, preprint (astro-ph/0512246)
- Ryu D., Ostriker J. P., Kang H., Cen R., 1993, *ApJ*, 414, 1
- Shakura N. I., Sunyaev R. A., 1973, *A&A*, 24, 337
- Shi J., Hu C., Shu C.-W., 2002, *Journal of Computational Physics*, 175, 108
- Shu C.-W., 1997, Technical report, Essentially Non-Oscillatory and Weighted Essentially Non-Oscillatory Schemes for Hyperbolic Conservation Laws, <http://hdl.handle.net/2002/14650>. NASA Langley Research Center
- Shu C.-W., Osher S., 1988, *Journal of Computational Physics*, 77, 439
- Shu C.-W., Osher S., 1989, *Journal of Computational Physics*, 83, 32
- Sod G. A., 1978, *Journal of Computational Physics*, 27, 1
- Spitkovsky A., 2006, *ApJ*, 648, L51
- Stone J. M., 2006, The Athena Test Suite, www.astro.princeton.edu/~jstone/tests
- Stone J. M., Norman M. L., 1992, *ApJS*, 80, 753
- Thompson J. F., Warsi Z. U., Mastin C. W., 1985, *Numerical grid generation: foundations and applications*. Elsevier North-Holland, Inc., New York, NY, USA
- Titarev V. A., Toro E. F., 2004, *Journal of Computational Physics*, 201, 238
- Toro E., 1997, *Riemann Solvers and Numerical Methods for Fluid Dynamics*. Springer-Verlag, Berlin, Heidelberg
- Toro E. F., Titarev V. A., 2006, *JCP*, pp 150–165
- Trac H., Pen U.-L., 2004, *New Astronomy*, 9, 443
- Wosley S. E., 1993, *ApJ*, 405, 273
- Xing Y., Shu C.-W., 2006, *Journal of Computational Physics*, 214, 567
- Zhang W., MacFadyen A. I., 2006, *ApJS*, 164, 255